Received: 31 August 2020 | Revised: 3 February 2021 | Accepted: 3 March 2021

DOI: 10.1002/nme.6666

RESEARCH ARTICLE

WILEY

3D formulation of the deformable discrete element method

Jerzy Rojek[1] | **Szymon Nosewicz**[1] | **Klaus Thoeni**[2]

[1]Institute of Fundamental Technological Research, Polish Academy of Sciences, Warsaw, Poland

[2]Centre for Geotechnical Science and Engineering, The University of Newcastle, Callaghan, Newcastle, Australia

Correspondence
Jerzy Rojek, Institute of Fundamental Technological Research, Polish Academy of Sciences, Pawinskiego 5B, Warsaw 02-106, Poland.
Email: jrojek@ippt.pan.pl

Funding information
Australian Research Council, Grant/Award Number: DP190102407; Narodowe Centrum Nauki, Grant/Award Number: DEC-2015/19/B/ST8/03983

Abstract

This work presents a 3D extension of the deformable discrete element method (DDEM) developed previously for 2D problems. The 3D formulation employs spherical particles. The particle deformation is made up of a global and local deformation mode. The global mode is assumed to be produced by uniform stress due to the contact forces. Particle deformability yields a nonlocal contact model, in which one contact between particles is influenced by contacts with other particles. It also leads to the formation of new contacts in the particle assembly. The DDEM affects the behavior of the granular material at the macroscopic level and gives new possibilities in material modeling by the discrete element method (DEM). The new algorithm is verified on a unconfined uniaxial compression test of a cuboid specimen discretized with equal-size bonded particles aligned in a simple cubic pattern using an analytical solution. Enhanced modeling capabilities are presented by simulating cylindrical specimens discretized with a nonuniform size of bonded particles. The micro–macro relationships for elastic parameters are obtained. It is shown that the DDEM extends the range of the Poisson's ratio achievable with the DEM. Additional simulations are performed to determine the stability limits of the DDEM.

KEYWORDS

average stress, deformable particles, discrete element method, elastic constants, micro–macro relationships, nonlocal contact model

1 | INTRODUCTION

The discrete element method (DEM) has become a valuable tool for predicting the behavior of various bonded and unbonded granular materials, for example, References 1-5. The DEM employs a model made up of particles called discrete elements interacting by contact. Although arbitrarily shaped particles can be used in the DEM, spheres are often chosen because of the simplicity and the computational efficiency of the numerical algorithm. The spherical discrete elements are also employed in this work. The contact between particles is considered using the so-called soft-contact approach, which follows the pioneering works of Cundall et al.[4,6,7] In this formulation, the contact nonpenetration conditions are satisfied approximately only. Particles are assumed rigid with a small overlap between contacting particles allowed. This overlap can be treated as equivalent to the deformation of the particles at the contact point. In contact models permitting tensile interaction, contact is also assumed for small gaps between particles. Contact models can be defined in terms of the particle overlap/gap and other kinetic and material parameters. In the standard DEM (SDEM), the contact is treated locally, that is, it is assumed that the contact between a pair of particles is not influenced by any other contact and it does not affect any other contact of the considered particles. Local treatment of the contact associated with particle nondeformability gives rise to some drawbacks of the DEM. Harthong et al.[8] have shown that a nonlocal contact model is needed for simulation of high-density compaction of granular materials. Some limitations in reproducing the macroscopic properties of granular material are another drawback of the DEM resulting from the assumption of particle nondeformability. Indeed, the SDEM formulation based on the soft-contact approach with rigid particles has limitations in reproducing the macroscopic behavior of materials with Poisson's ratio greater than 1/3 in 2D and 1/4 in 3D DEM models.[9]

It has been shown in many publications that deformability of discrete elements mitigates the DEM drawbacks and improves its modeling capabilities. Deformability can be introduced into the DEM by discretizing the discrete elements with finite elements.[8,10] Using this approach, Munjiza[11] developed the combined finite discrete element method which was used to solve static and dynamic behavior of systems of solid deformable bodies. Particle discretization can also be performed using other discretization methods, for instance, the continuum-based material point method[12,13] or the discrete-based bonded particle method.[12,14] The methods based on the discretization of particles (discrete elements) can be used to model particles of arbitrary shapes and different deformation mechanisms assuming the elastic or plastic behavior of deformable particles. It is also possible to model the breakage of particles. However, a high computational cost of such an approach impedes its use for a large particle number.

Another way to consider deformability of discrete elements consists in adding deformation modes to rigid motion of discrete elements. Cundall et al.[15] presented the formulation for a discontinuous system of deformable blocks (triangular or quadrilateral prisms) describing the block deformation by superposition of independent strain modes. This concept is implemented into the commercial codes UDEC and 3DEC.[16] In 3DEC, deformable blocks are discretized into tetrahedral, constant-strain zones, which are equivalent to constant-strain finite elements. Williams and Mustoe[17] proposed that the deformation of discrete elements can be given in terms of a set of orthogonal modes which may or may not be eigenmodes. Eigenmodes obtained from the modal analysis were used as the basis to describe the deformation of a discrete element by Jin et al.[18] Another method based on discrete modeling is discontinuous deformation analysis (DDA) developed by Shi.[19] The displacement field in the DDA is described in terms of polynomial functions. The main difference between the DDA and the DEM formulations referenced here lies in the solution scheme. The DEM equations are integrated in time using an explicit scheme while the DDA employs an implicit solution algorithm which requires the evaluation of the stiffness matrices of the deformable blocks.

The above referenced formulations[11,15,17-19] deal with deformable blocks— polygons (in 2D) or polyhedra (in 3D). There are only few works incorporating deformability of cylindrical (in 2D) or spherical (in 3D) discrete elements. A simple method to consider deformability of spherical discrete elements has been presented by Brodu et al.[20] who proposed the so-called multiple-contact discrete element method, in which the overlap at a contact point is corrected using the analytical solution of the elasticity problem of a sphere subjected to a contact force at another point. Thus, a nonlocal contact model with reciprocal dependence of the contacts has been obtained. Simultaneous action and dependence of contacts have also been considered in the so-called granular element method proposed by Karanjgaokar.[21]

An original formulation of the DEM with deformable cylindrical particles, named the deformable discrete element method (DDEM), has been developed by Rojek et al.[22] It has been assumed that the particles are deformed globally due to the internal stress produced by the contact forces. The particle averaged stress has been taken as the internal particle stress. A global particle deformation has been obtained from the particle stress using the elastic compliance matrix. The global deformation is accounted for in the evaluation of the particle overlap, which is used in the calculation of the contact force. Therefore, a nonlocal contact model has been obtained. It has also been shown in Reference 22 that the DDEM allows obtaining a broader range of the macroscopic Poisson's ratio in comparison to the SDEM. Numerical properties of the algorithm of the DDEM with circular discs have been investigated thoroughly by Madan et al.[23] It has been shown that the explicit DDEM algorithm is conditionally stable. Its stability is restricted by the critical time step, which is the same as in the SDEM, and by the convergence criterion of the iterative solution of the contact forces.

This article presents an extension of the original 2D DDEM to 3D. The 3D formulation employs spherical particles which are treated as deformable discrete elements. The 3D algorithm of the DDEM has been implemented in the same way as it was described for 2D problems in Reference 22. The basic features of the DDEM previously revealed in 2D analyses have now been investigated in 3D problems. The results confirm enhancement of the modeling features of the DEM when deformability of discrete elements is considered. In particular, it extents the range of the macroscopic Poisson's ratio. The present work shows new possibilities to use the DDEM in simulations of real problems which usually require 3D modeling.

The outline of the article is as follows. The basic equations of the standard formulation of the DEM are provided in Section 2 in order to enable a complete definition of the models used in this work. Basic assumptions and the algorithm of the 3D DDEM are presented in Section 3. General criteria for the convergence and stability of the DDEM solution scheme are discussed in Section 3.7. Averaging procedures for macroscopic stress and strains and derivation of micro–macro constitutive relationships in the DEM and DDEM are introduced in Section 4. Section 5 presents verification of the DDEM. Unconfined uniaxial compression of a cuboid specimen discretized according to the simple cubic (SC) pattern has been simulated in Section 5.1. The results obtained in the simulations have been compared with the analytical solution presented in Appendix A. Two different cylindrical specimens discretized with nonuniform sized particles have been used in Section 5.2 to simulate unconfined uniaxial compression to show the performance of the DDEM. Micro–macro relationships for the constitutive elastic properties have been obtained. A broader range of macroscopic elastic moduli demonstrates advantages of the DDEM. Finally, the stability of the DDEM solution is investigated numerically in Section 6 and conclusions are provided in Section 7.

2 | FORMULATION OF THE SDEM

2.1 | Equations of motion

The motion of an arbitrarily shaped discrete element is governed by the Newton–Euler rigid body dynamics equations. The translational motion of the ith element is described in the inertial reference frame by the Newton equation:

$$m_i \ddot{\mathbf{r}}_i = \mathbf{f}_i, \tag{1}$$

where $\mathbf{r}_i$ is the position of the center of mass of the discrete element i in the inertial reference frame, m_i is the mass of element i, and $\mathbf{f}_i$ is the resultant force acting on element i. The rotational motion is conveniently described by the Euler equation in the moving body-fixed coordinate system with the origin at the center of mass:[24]

$$\mathbf{J}_i \dot{\boldsymbol{\omega}}_i + \boldsymbol{\omega}_i \times \mathbf{J}_i \boldsymbol{\omega}_i = \mathbf{T}_i, \tag{2}$$

where $\boldsymbol{\omega}_i$ is the angular velocity relative to the inertial reference frame, $\mathbf{J}_i$ the inertia tensor in the body-fixed reference system, and $\mathbf{T}_i$ the resultant moment about the axes of the moving reference system. The main advantage of the body-fixed reference system is the constant inertia tensor which greatly simplifies the description. Further simplification can be obtained if the axes of the rotating reference system coincide with principal axes of inertia. Then the tensor is represented by a diagonal matrix.

This work considers spherical discrete elements. For spherical particles the second term in Equation (2) vanishes and the equation of rotational motion simplifies to the following form:

$$J_i \dot{\boldsymbol{\omega}}_i = \mathbf{T}_i, \tag{3}$$

where J_i is the moment of inertia of a sphere. The moment of inertia of a sphere is equal for all the central axes. Hence, Equation (3) can be used by taking the moving reference frame with the origin at the center of mass and the axes parallel to the fixed inertial frame.

Although the spheres after deformation become ellipsoids, it is assumed that the deformation is small and the deformed particles can be treated as spheres in the description of the rotational motion. Therefore, the rotational equation can still be described by Equation (3).

The resultant force $\mathbf{f}_i$ in Equation (1) includes the external load $\mathbf{f}_i^{\mathrm{ext}}$, all the contact forces with other particles $\mathbf{f}^{\mathrm{c}}$ and the external damping force $\mathbf{f}_i^{\mathrm{damp}}$:

$$\mathbf{f}_i = \mathbf{f}_i^{\mathrm{ext}} + \sum_{c=1}^{n_i^{\mathrm{c}}} \mathbf{f}^{\mathrm{c}} + \mathbf{f}_i^{\mathrm{damp}}, \tag{4}$$

where n_i^{c} is the number of contact points with other particles. The resultant moment $\mathbf{T}_i$ in Equation (3) comprises moments due to the contact forces $\mathbf{f}^{\mathrm{c}}$ and the external damping moment $\mathbf{T}_i^{\mathrm{damp}}$:

$$\mathbf{T}_i = \sum_{c=1}^{n_i^{\mathrm{c}}} \mathbf{s}^{\mathrm{c}} \times \mathbf{f}^{\mathrm{c}} + \mathbf{T}_i^{\mathrm{damp}}, \tag{5}$$

where $\mathbf{s}^{\mathrm{c}}$ is the vector connecting the center of the ith particle with the contact point (Figure 1).

Nonviscous damping is used and the damping terms $\mathbf{f}_i^{\text{damp}}$ and $\mathbf{T}_i^{\text{damp}}$ are evaluated as follows:

$$\mathbf{f}_i^{\text{damp}} = -\alpha^{\text{t}} \left\| \mathbf{f}_i^{\text{ext}} + \sum_{c=1}^{n_i^{\text{c}}} \mathbf{f}^{\text{c}} \right\| \frac{\dot{\mathbf{r}}_i}{\|\dot{\mathbf{r}}_i\|}, \tag{6}$$

$$\mathbf{T}_i^{\text{damp}} = -\alpha^{\text{r}} \left\| \sum_{c=1}^{n_i^{\text{c}}} \mathbf{s}^{\text{c}} \times \mathbf{f}^{\text{c}} \right\| \frac{\boldsymbol{\omega}_i}{\|\boldsymbol{\omega}_i\|}. \tag{7}$$

where α^{t} and α^{r} are the translational and rotational damping factors, respectively.

2.2 | Contact model

The elastic perfectly brittle model of the contact interaction between initially bonded particles is used in the present work. The rheological scheme of the contact model is shown in Figure 2.

This scheme corresponds to the decomposition of the contact force $\mathbf{f}^{\text{c}}$ into the normal and tangential components, $\mathbf{f}_{\text{n}}$ and $\mathbf{f}_{\text{t}}$, respectively:

$$\mathbf{f}^{\text{c}} = \mathbf{f}_{\text{n}} + \mathbf{f}_{\text{t}} = f_{\text{n}}\mathbf{n} + \mathbf{f}_{\text{t}}, \tag{8}$$

with $\mathbf{n}$ being the unit normal vector at the contact point (Figure 1). The Kelvin–Voigt models consisting of a spring and damper are used for the normal and tangential contact interaction. Accordingly, the contact force components consist of elastic parts, f_{ne} and $\mathbf{f}_{\text{te}}$, and damping parts, f_{nd} and $\mathbf{f}_{\text{td}}$:

$$f_{\text{n}} = f_{\text{ne}} + f_{\text{nd}} \tag{9}$$

$$\mathbf{f}_{\text{t}} = \mathbf{f}_{\text{te}} + \mathbf{f}_{\text{td}} \tag{10}$$

The linear model is assumed for elastic contact force components. The elastic normal force is given by

$$f_{\text{ne}} = k_{\text{n}} h, \tag{11}$$

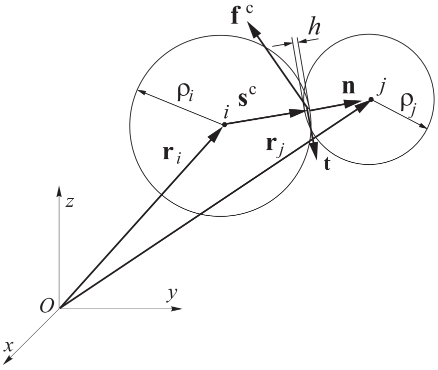

FIGURE 1 Definition of interparticle interaction

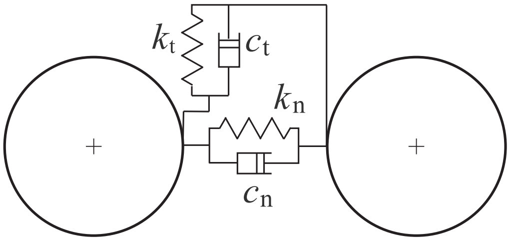

FIGURE 2 Contact model

where k_n is the normal contact stiffness, and h is the overlap ($h \leq 0$) or the gap ($h > 0$) between particles given by

$$h = ||\mathbf{r}_j - \mathbf{r}_i|| - \rho_i - \rho_j, \tag{12}$$

where ρ_i and ρ_j denote the radii of the particles. The tangential elastic force $\mathbf{f}_{te}$ must be evaluated incrementally, cf. References 25,26:

$$\mathbf{f}_{te} = \mathbf{f}_{te}^{old} + \Delta\mathbf{f}_{te}, \tag{13}$$

where $\mathbf{f}_{te}^{old}$ is the vector of the force from the previous time step rotated to the present contact plane and its increment $\Delta\mathbf{f}_{te}$ is given by:

$$\Delta\mathbf{f}_{te} = k_t \ \Delta\mathbf{u}_t = k_t\mathbf{v}_{rt}\Delta t, \tag{14}$$

where k_t is the tangential contact stiffness, $\Delta\mathbf{u}_t$ the incremental relative tangential displacement, $\mathbf{v}_{rt}$ the relative tangential velocity at the contact point and Δt the time step.

The normal and tangential damping forces are given by

$$f_{nd} = c_n v_{rn}, \tag{15}$$

and

$$\mathbf{f}_{td} = c_t\mathbf{v}_{rt}, \tag{16}$$

respectively, where c_n and c_t are the damping coefficients in the normal and tangential direction, which are evaluated by scaling the critical damping factors, c_n^{cr} and c_t^{cr}, by corresponding factors, ξ_n and ξ_t:

$$c_n = \xi_n c_n^{cr} \tag{17}$$

$$c_t = \xi_t c_t^{cr} \tag{18}$$

The critical damping c^{cr} for two particles connected with a spring is given by, cf. Reference 27:

$$c^{cr} = 2\sqrt{\frac{m_i m_j k}{m_i + m_j}}, \tag{19}$$

where m_i and m_j correspond to the particle masses and k to the spring stiffness. The critical damping factors c_n^{cr} and c_t^{cr} can be obtained substituting $k = k_n$ or k_t into Equation (19).

The bonds between particles break instantaneously when the contact force either in the normal or tangential direction exceeds the respective interface strength, ϕ_n or ϕ_t:

$$f_n \geq \phi_n, \tag{20}$$

$$||\mathbf{f}_t|| \geq \phi_t. \tag{21}$$

After a bond is broken, frictional contact with Coulomb friction is assumed.

3 | FORMULATION OF THE DDEM

3.1 | Basic assumptions

The DDEM considers an assembly of deformable spherical particles. It is assumed that the particle deformation consists of a global and a local deformation mode. The global deformation is defined by uniform strain induced by the particle stresses resulting from the contact forces. The local deformation is assumed to be represented by an overlap/gap of the globally deformed particles. This overlap is used in the calculation of the normal contact force.

3.2 | Particle stresses

The average stress $\boldsymbol{\sigma}_p$ in a particle (Figure 3) subjected to loading by n_{pc} contact forces $\mathbf{f}^c$ is given by, cf. References 28,29:

$$\boldsymbol{\sigma}_p = \frac{1}{V_p} \sum_{c=1}^{n_{p\,c}} \mathbf{s}^c \otimes \mathbf{f}^c, \tag{22}$$

where V_p is the particle volume and $\mathbf{s}^c$ is the vector connecting the particle center with the contact point. The symbol $\otimes$ denotes the outer (tensor) product. By writing the vectors $\mathbf{s}^c$ and $\mathbf{f}^c$ in their component form $\mathbf{s}^c = \{s_x^c, s_y^c, s_z^c\}^T$ and $\mathbf{f}^c = \{f_x^c, f_y^c, f_z^c\}^T$, respectively, the stress evaluated according to Equation (22) can be expressed in the following matrix form:

$$\boldsymbol{\sigma}_p = \begin{bmatrix} (\sigma_p)_{xx} & (\sigma_p)_{xy} & (\sigma_p)_{xz} \\ (\sigma_p)_{yx} & (\sigma_p)_{yy} & (\sigma_p)_{yz} \\ (\sigma_p)_{zx} & (\sigma_p)_{zy} & (\sigma_p)_{zz} \end{bmatrix} = \frac{1}{V_p} \sum_{c=1}^{n_{pc}} \begin{bmatrix} s_x^c f_x^c & s_x^c f_y^c & s_x^c f_z^c \\ s_y^c f_x^c & s_y^c f_y^c & s_y^c f_z^c \\ s_z^c f_x^c & s_z^c f_y^c & s_z^c f_z^c \end{bmatrix}. \tag{23}$$

3.3 | Particle strains

The small strain tensor $\boldsymbol{\varepsilon}_p$ describing the particle global deformation is calculated using the inverse constitutive relationship:

$$\boldsymbol{\varepsilon}_p = \mathbf{D}_p : \boldsymbol{\sigma}_p, \tag{24}$$

where $\mathbf{D}_p$ is the elastic compliance tensor. The strain–stress relation can be written in matrix notation as:

$$\tilde{\boldsymbol{\varepsilon}}_p = \tilde{\mathbf{D}}_p \tilde{\boldsymbol{\sigma}}_p, \tag{25}$$

where the strain and stress tensors are represented by the vectors $\tilde{\boldsymbol{\varepsilon}}_p = \{(\varepsilon_p)_{xx}, (\varepsilon_p)_{yy}, (\varepsilon_p)_{zz}, (\varepsilon_p)_{xy}, (\varepsilon_p)_{yz}, (\varepsilon_p)_{xz}\}^T$ and $\tilde{\boldsymbol{\sigma}}_p = \{(\sigma_p)_{xx}, (\sigma_p)_{yy}, (\sigma_p)_{zz}, \sigma_p)_{xy}, (\sigma_p)_{yz}, (\sigma_p)_{xz}\}^T$, respectively, and $\tilde{\mathbf{D}}_p$ is the elastic compliance matrix given as follows:

$$\tilde{\mathbf{D}}_p = \frac{1}{E_p} \begin{bmatrix} 1 & -\nu_p & -\nu_p & 0 & 0 & 0 \\ -\nu_p & 1 & -\nu_p & 0 & 0 & 0 \\ -\nu_p & -\nu_p & 1 & 0 & 0 & 0 \\ 0 & 0 & 0 & 1+\nu_p & 0 & 0 \\ 0 & 0 & 0 & & 1+\nu_u & 0 \\ 0 & 0 & 0 & 0 & 0 & 1+\nu_p \end{bmatrix}, \tag{26}$$

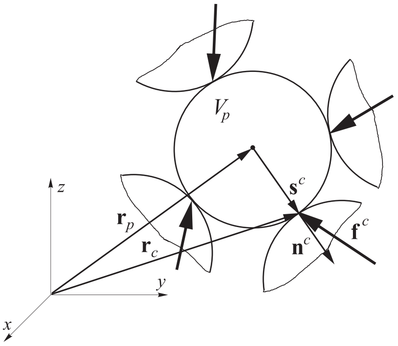

FIGURE 3 Vectors used in the particle stress evaluation

where E_p and ν_p are the Young's modulus and the Poisson's ratio of the particles, respectively. Both, stress $\boldsymbol{\sigma}_p$ and strain $\boldsymbol{\varepsilon}_p$, are homogenous within the particle.

3.4 | Particle global deformation mode

By setting the displacements at the particle center $\mathbf{r}_p$ to zero and taking advantage of the assumption that the strain in the particle $\boldsymbol{\varepsilon}_p$ is constant, the displacement u of an arbitrary point r of the particle is given by Reference 30:

$$\mathbf{u}(\mathbf{r}) = \boldsymbol{\varepsilon}_\mathbf{p}(\mathbf{r} - \mathbf{r}_\mathbf{p}), \tag{27}$$

where $\boldsymbol{\varepsilon}_p$ is the strain matrix

$$\boldsymbol{\varepsilon}_p = \begin{bmatrix} (\varepsilon_p)_{xx} & (\varepsilon_p)_{xy} & (\varepsilon_p)_{xz} \\ (\varepsilon_p)_{xy} & (\varepsilon_p)_{yy} & (\varepsilon_p)_{yz} \\ (\varepsilon_p)_{xz} & (\varepsilon_p)_{yz} & (\varepsilon_p)_{zz} \end{bmatrix}. \tag{28}$$

The displacement field $\mathbf{u}(\mathbf{r})$, with $r \in V_p$, defines the global deformation of the particle. The sphere is homogenously deformed into an ellipsoid whose principal axes are along the principal strain directions. Since small global particle deformation is assumed, the change in particle shape can be neglected in the evaluation of the inertia tensor and in the averaged stress calculation, whereas it is taken into account in the determination of the contact between the particles.

3.5 | Contact detection and contact force evaluation

The contact between a pair of particles (Figure 4(A)) is established according to the value of the overlap/gap h_c between globally deformed particles. h_c is evaluated modifying the overlap h in the SDEM given by Equation (12) by projecting the vectors of the displacements of the contact points of both particles $\mathbf{u}_c^i$ and $\mathbf{u}_c^j$ on the outward normal unit vectors $\mathbf{n}_c^i$ and $\mathbf{n}_c^j$ (see Figure 4(B))

$$h_c \approx h + \mathbf{u}_c^i \cdot \mathbf{n}_c^i + \mathbf{u}_c^j \cdot \mathbf{n}_c^j \tag{29}$$

having in mind that $\mathbf{n}_c^i = -\mathbf{n}_c^j = \mathbf{n}_c$. The displacements $\mathbf{u}_c^a$, with $a = i,j$, are evaluated substituting $\mathbf{r} = \mathbf{r}_c^a$, with $a = i,j$, in Equation (27):

$$\mathbf{u}_c^a = \boldsymbol{\varepsilon}_p^a(\mathbf{r}_c^a - \mathbf{r}_p^a). \tag{30}$$

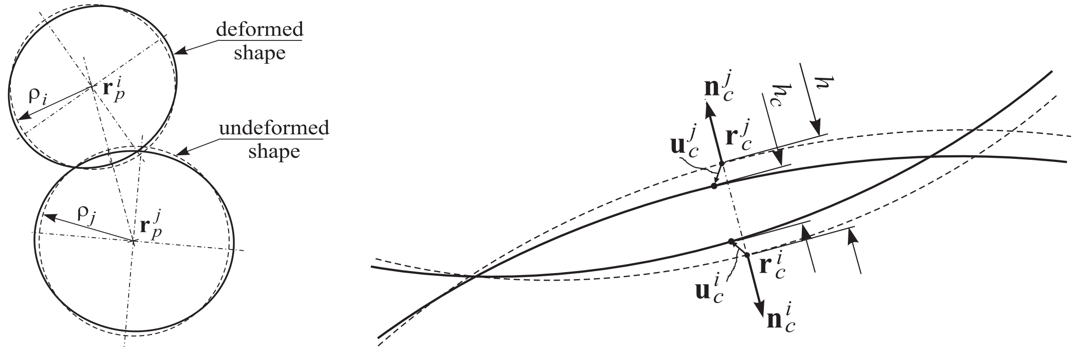

(A) (B)

FIGURE 4 Two deformable particles in contact: (A) Overview and (B) details at the contact point

Equation (29) is valid for both compressive and tensile contact (for both $h_c \leq 0$ and $h_c > 0$). Replacing the parameter h in Equation (11) by h_c, the elastic contact force f_{ne} is now evaluated as:

$$f_{\mathrm{ne}} = k_{\mathrm{n}} h_c. \tag{31}$$

It is assumed that the normal and tangential directions at the contact point are unaffected by the deformation and that the offset of the contact point with respect to the line connecting the particle centers is negligibly.

3.6 | Solution algorithm

The calculation of the contact forces in the DDEM requires not only the positions of contacting particles but also knowledge of the particle strains which depend on other contact forces in the particle assembly. This dependence can be written as an implicit relationship for all the contact forces in the particle system

$$\mathbf{F}_c = \boldsymbol{\mathcal{F}}(\mathbf{R}, \mathbf{E}(\mathbf{F}_c)), \tag{32}$$

where $\mathbf{F}_c$, $\mathbf{R}$, and $\mathbf{E}$ are the global vectors containing all the contact forces $\mathbf{f}_c^j$, particle positions $\mathbf{r}_p^i$ and particle strains $\tilde{\boldsymbol{\varepsilon}}_p^i$:

$$\mathbf{F}_c = \{\mathbf{f}_c^j, \ \dots \ , \mathbf{f}_c^{N_c}\}^T, \tag{33}$$

$$\mathbf{R} = \{\mathbf{r}_p^i, \ \dots \ , \mathbf{r}_p^{N_p}\}^T, \tag{34}$$

$$\mathbf{E} = \{\tilde{\boldsymbol{\varepsilon}}_p^i, \ \dots \ , \tilde{\boldsymbol{\varepsilon}}_p^{N_p}\}^T, \tag{35}$$

where N_p is the number of particles and N_c the number of contacts in the particle assembly.

In a general case, solving the problem given by Equation (32) would require an iterative solution scheme:

$$\mathbf{F}_c^{(n,k+1)} = \boldsymbol{\mathcal{F}}(\mathbf{R}^{(n)}, \mathbf{E}(\mathbf{F}_c^{(n,k)})), \tag{36}$$

where the superscript n denotes the nth time step, and the superscripts k and $k+1$ subsequent iterations. The iterations should be performed at each time step, which would be inconsistent with the noniterative explicit time integration used in the SDEM. Therefore, similarly as in the 2D formulation of the DDEM in Reference 22, the implementation of the 3D DDEM follows a simplified algorithm where iterations are combined with the time-stepping procedure for the equations of motion. The solution algorithm employs the explicit dependence

$$\mathbf{F}_c^{(n)} = \boldsymbol{\mathcal{F}}(\mathbf{R}^{(n)}, \mathbf{E}(\mathbf{F}_c^{(n-1)})) \tag{37}$$

and the calculation of the contact forces at the nth time step is performed using the strains corresponding to the contact forces from the previous time step.

The 3D DDEM algorithm has been implemented in the author's in-house version of the discrete element program DEMPack validated earlier for different applications, cf. References 31-33.

3.7 | Convergence and stability of the DDEM algorithm

It has been shown in Reference 23 that the stability of the explicit DDEM solution scheme is conditionally stable. The stability is restricted by the critical time step of the explicit time integration and the convergence limit of the iterative solution of an implicit relationship given by Equation (37). It has also been demonstrated in Reference 23 that the critical time step for the DDEM remains unchanged with respect to the SDEM. To establish the convergence criterion of the iterative scheme, the general form of the iterative scheme presented in Equation (37) is transformed into the following recursive relationship for the successive differences between the approximations of the contact forces, cf. Reference 23:

$$\mathbf{F}_c^{(n,k+1)} - \mathbf{F}_c^{(n,k)} = \mathbf{B}\,(\mathbf{F}_c^{(n,k)} - \mathbf{F}_c^{(n,k-1)}). \tag{38}$$

The convergence condition of the iterative scheme defined by Equation (38) can be expressed in terms of the matrix spectral radius ρ of the iteration matrix **B**, cf. Reference 34:

$$\rho(\mathbf{B}) < 1. \tag{39}$$

The spectral radius $\rho(\mathbf{B})$ is defined as

$$\rho(\mathbf{B}) = \max_{\lambda \in \Phi(\mathbf{B})} |\lambda|, \tag{40}$$

where λ is the eigenvalue of **B** and $\Phi(\mathbf{B})$ denotes the set of eigenvalues of **B**. If the condition in Equation (39) is satisfied, the iterative error given by the norms of successive differences decreases

$$\frac{||\mathbf{F}_c^{(n,k+1)} - \mathbf{F}_c^{(n,k)}||}{||\mathbf{F}_c^{(n,k)} - \mathbf{F}_c^{(n,k-1)}||} < 1. \tag{41}$$

The criterion expressed by Equation (39) has been used in the present work to determine the theoretical convergence condition for the regular cubic configuration of spherical particles.

4 | MICRO–MACRO RELATIONSHIPS

The macroscopic behavior of particulate material represented by an assembly of discrete elements can be described in terms of averaged macroscopic stress and strain tensors coupled by certain equivalent macroscopic constitutive relationships. The objective of the present work is to establish macroscopic constitutive relationships for the DDEM in the elastic range. Evaluation of the effective macroscopic stress and strain tensors, $\overline{\sigma}_{ij}$ and $\overline{\varepsilon}_{ij}$, respectively, and effective macroscopic elastic constants will be presented below.

4.1 | Macroscopic stress and strain tensor

The average macroscopic stress $\overline{\boldsymbol{\sigma}}$ in the specimen can be obtained using an averaging formula, cf. Reference 35:

$$\overline{\boldsymbol{\sigma}} = \frac{1}{V}\sum_{c=1}^{N_c} \mathbf{L}^c \otimes \mathbf{f}^c, \tag{42}$$

where N_c is the number of all the contacts in the volume V, and $\mathbf{L}^c$ is the vector connecting the centers of two contacting particles.

The average macroscopic strain tensor in the specimen has been obtained according to the method developed by Bagi.[36] First, a mesh of tetrahedra is generated over the centers of the particles in the specimen. The average strain tensor $\overline{\boldsymbol{\varepsilon}}$ in the whole specimen is obtained as a weighted average of the strains $\boldsymbol{\varepsilon}^k$ in the tetrahedral cells

$$\overline{\boldsymbol{\varepsilon}} = \frac{1}{V}\sum_{k} V_k \boldsymbol{\varepsilon}^k, \tag{43}$$

where V_k is the volume of an elementary cell. The strains $\boldsymbol{\varepsilon}^k$ are determined in terms of the particle displacements, for more details see Reference 36.

4.2 | Macroscopic elastic moduli based on Voigt's hypothesis

Applying Voigt's hypothesis to the assembly of equal sized particles of the same material the following analytical formulae can be derived for the average macroscopic elastic moduli, Young's modulus E and Poisson's ratio ν, cf. References 9,37:

$$E = \frac{4N_c\rho^2 k_n}{3V} \cdot \frac{2 + 3k_t/k_n}{4 + k_t/k_n} \tag{44}$$

$$\nu = \frac{1 - k_t/k_n}{4 + k_t/k_n} \tag{45}$$

where N_c is the total number of interparticle contacts in the volume V, ρ is the particle radius, k_n and k_t are the normal and tangential contact stiffnesses, respectively. Introducing the coordination number n_c

$$n_c = \frac{2N_c}{N_p}, \tag{46}$$

where N_p is the number of particles, and expressing the specimen volume V as

$$V = \frac{4\pi N_p \rho^3}{3(1 - e)}, \tag{47}$$

where e is the specimen porosity, Equation (44) can be rewritten in the following form:

$$E = \frac{n_c(1 - e)k_n}{2\pi\rho} \cdot \frac{2 + 3k_t/k_n}{4 + k_t/k_n}. \tag{48}$$

4.3 | Dimensionless constitutive relationships

Micro–macro constitutive relationships in the DEM are often derived in the framework of dimensional analysis.[38-40] In the SDEM, the dimensionless relationships for the Young's modulus E and the Poisson's ratio ν can be postulated in the following form, cf. Reference 41:

$$\frac{E\overline{\rho}}{k_n} = \Phi_E\left(\frac{k_t}{k_n}, \Psi\right), \tag{49}$$

$$\nu = \Phi_\nu\left(\frac{k_t}{k_n}, \Psi\right), \tag{50}$$

where $\overline{\rho}$ is the average particle radius, and Φ_E and Φ_ν are the scaling functions for the elastic constants. The latter are assumed to be functions of the ratio k_t/k_n and of a certain function Ψ representing the geometrical characteristics of the assembly, taking into account the influence of other parameters such as porosity, particle size distribution, coordination number, and so forth. The dimensionless relationships in Equations (49) and (50) hold for a specific assembly of particles with given geometric characteristics.

Taking advantage of Equations (45) and (48), the dimensionless scaling functions for the elastic constants can be redefined as follows:[41]

$$\frac{E\overline{\rho}}{k_n n_c(1 - e)} = \hat{\Phi}_E\left(\frac{k_t}{k_n}\right), \tag{51}$$

$$\nu = \hat{\Phi}_\nu\left(\frac{k_t}{k_n}\right). \tag{52}$$

In the DDEM, the dimensional analysis should also include the particle Poisson's ratio ν_p and the particle Young's modulus E_p.[22] The following dimensionless relationships for the elastic constants can be postulated in the DDEM as:

$$\frac{E\overline{\rho}}{k_n n_c(1 - e)} = \hat{\Phi}_E\left(\frac{k_t}{k_n}, \frac{k_n}{E_p\overline{\rho}}, \nu_p\right), \tag{53}$$

$$\nu = \hat{\Phi}_\nu\left(\frac{k_t}{k_n}, \frac{k_n}{E_p\overline{\rho}}, \nu_p\right). \tag{54}$$

Specific forms of Equations (53) and (54) will be obtained later carrying out a series of simulations of the uniaxial compression test. The effect of particle deformability on the elastic constants will be analyzed comparing Equations (53) and (54) with Equations (51) and (52) obtained using the SDEM. Theoretical Equations (44) and (45) will verify the results of the SDEM analyses. Equations (44), (45), (51), (52), (53), and (54) should be valid for particle assemblies with different geometric characteristics. This validity will be checked using two different specimens in the numerical simulations.

5 | NUMERICAL VERIFICATION

5.1 | Uniaxial compression of a cuboid sample with SC packing

Unconfined uniaxial compression of a cuboid specimen discretized with $9 \times 9 \times 20 = 1620$ bonded spheres aligned regularly according to a SC pattern (Figure 5(A)) has been simulated with the standard and DDEM formulations. The spherical particles are equal in size with a radius $\rho = 1$ mm. The model parameters are as follows: density $d = 9899$ kg/m^3, normal contact stiffness $k_n = 1 \cdot 10^8$ N/m, $k_t/k_n = 0.1$. The model with deformable particles has been studied taking into account different values of the particle Young's modulus E_p ($1.5 \cdot 10^{11}$, $2.0 \cdot 10^{11}$, and $2.5 \cdot 10^{11}$ N/m^2) and constant particle Poisson's ratio $\nu_p = 0.33$. This example demonstrates the enhancement of the DDEM in reproducing the Poisson's effect and verifies the formulation and numerical algorithm of the DDEM by comparing the numerical results to the analytical solution of the static problem.

The sample has been uniaxially compressed under a uniform load represented by equal forces F applied in z-direction at the particles of the top layer, as shown in Figure 5(A). The bottom-layer particles have been restrained in z-direction and are free to move in the other two directions, x and y. The symmetry conditions have been applied to the particles in the planes of symmetry $x = 0$ and $y = 0$. The evolution of the loading is shown in Figure 5(B). The forces F have been increasing linearly from 0 to $F_{\max} = 10$ kN during the interval $t = 0$ to $t_{\text{load}} = 1$ ms and then kept constant until $t_{\text{end}} = 1.2$ ms.

Quasi-static loading conditions and a linear response have been ensured by considering adequate damping. A damping coefficient of $\xi^n = 1.3$ has been used. The damping coefficient ξ^n introduced in Equation (17) defines the damping parameter c_n with respect to the critical damping c_n^{cr} for a pair of particles given by Equation (19).

Figures 6 and 7 show the results obtained with the SDEM and DDEM formulations, respectively, in the form of the contours of displacements along the x, y, and z axes at the final stage of loading. It can be seen in Figure 6(B,C) that all the particles in the SDEM solution have zero lateral displacements. On the contrary, the x and y displacements in the DDEM solution in Figure 7(B,C) are nonzero, which shows that the new formulation is capable to represent the Poisson's effect even in such a simple configuration of spheres.

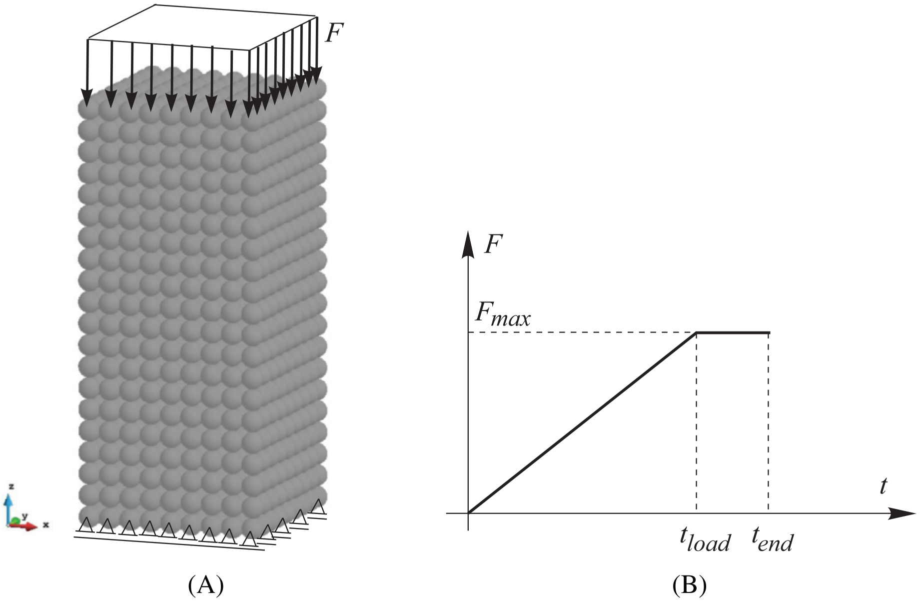

(A) (B)

FIGURE 5 Unconfined uniaxial compression of a cuboid sample: (A) discrete element model and (B) loading force versus time

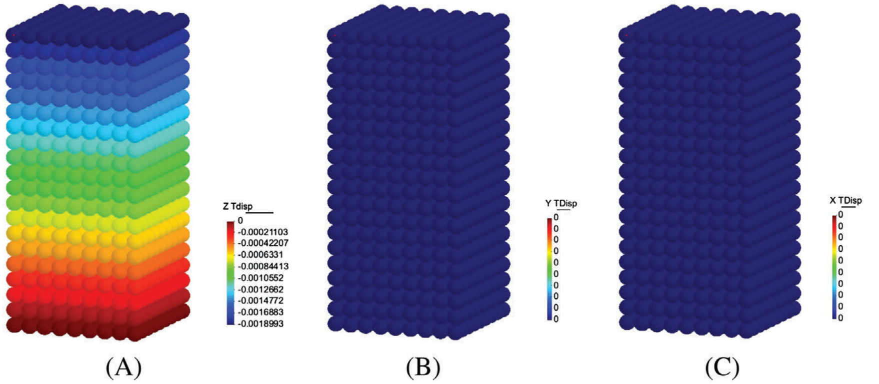

FIGURE 6 Simulation results obtained using the standard discrete element method formulation—contours of displacements (in meters) along: (A) the z-axis, (B) the y-axis, (C) the x-axis at $t = 1.2$ ms, $k_n = 10^8$ N/m, $k_t/k_n = 0.0$, $\alpha_d = 1.3$

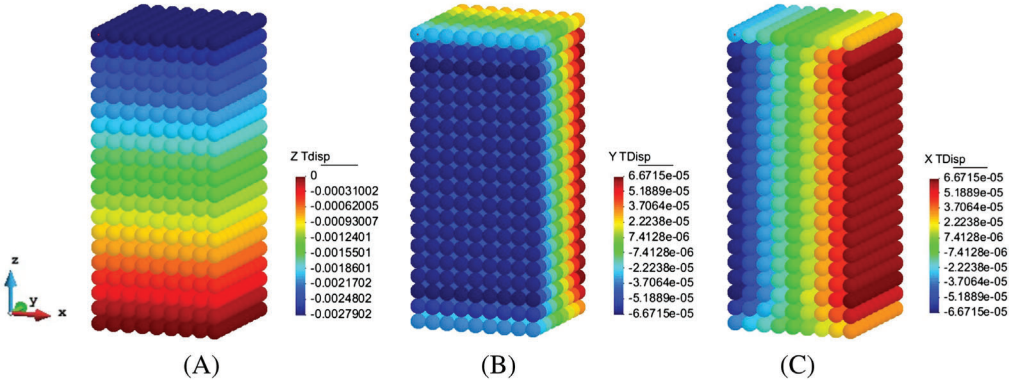

FIGURE 7 Simulation results obtained using the deformable discrete element method formulation—contours of displacements (in meters) along: (A) the z-axis, (B) the y-axis, (C) the x-axis at $t = 1.2$ ms, $k_n = 10^8$ N/m, $k_t/k_n = 0.0$, $E_p = 2 \cdot 10^{11}$, $\nu_p = 0.33$, $\alpha_d = 1.3$, $k_n/(E_p \rho) = 0.5$

The specimen response has been characterized in Figure 8 by plots of evolution of displacement of loaded top-layer particles in the SDEM and DDEM models. The response is almost linear during the initial linearly increasing loading stage. This indicates that the quasi-static conditions should be captured correctly. The quasi-static regime in the DEM simulations of granular flows is often checked quantitatively by the inertial number.[42] In this work, we deal with the system of bonded particles, so a better indicator of quasi-static conditions can be the ratio of the kinetic and internal energy which is commonly used in explicit FEM simulations of quasi-static problems.[43,44] It is commonly accepted that a solution can be considered quasi-static if the ratio kinetic energy to internal energy in the system is less than 0.05 for most of the time.[43,44] Figure 9 shows plots of the ratio between kinetic energy and internal (elastic strain) energy during compression of the cuboid sample. It can be observed that except for a very short initial stage this ratio is very small and much lower than 0.05. This confirms that the response obtained in the presented simulations can be considered as quasi-static.

The displacements in the DDEM models in Figure 8 are higher than in the SDEM model which indicates that the deformability of the particles softens the macroscopic stiffness of the discrete material. The effect of the particle properties on the effective stiffness is also shown. It can be seen that the lower the Young's modulus of the particle E_p (or equivalently, the higher the ratio $k_n/(E_p \rho)$) the lower the global stiffness in the DDEM, which is manifested by larger deformations.

Both SDEM and DDEM results in Figure 8 have been compared with the corresponding analytical solutions. The numerical predictions agree very well with the analytical results. The analytical solutions for the three cases of the DDEM model have been obtained using the procedure presented in Appendix A. The key values are summarized in Table 1.

The lateral deformation of the specimen can be characterized by the displacements of the nodes on the specimen sides either in x or y direction. The lateral displacements of the representative point in the center of one of the sides have been plotted as a function of time for different values of Young's modulus (Figure 10). Similarly as for the case of the displacement in the loading direction, it can be seen that the lower the Young's modulus of the particles E_p (or equivalently, the higher the ratio $k_n/(E_p \rho)$), the larger the lateral displacement. The numerical predictions in Figure 10

FIGURE 8 Evolution of the displacement in the loading direction—comparison of the SDEM and DDEM solutions, $k_n = 10^8$ N/m, $\nu_p = 0.33$. DDEM, deformable discrete element method; SDEM, standard discrete element method

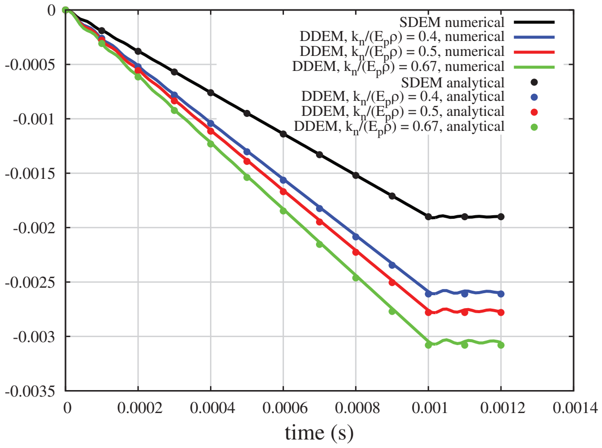

FIGURE 9 Ratio of kinetic energy to elastic strain energy in compression of the cuboid sample

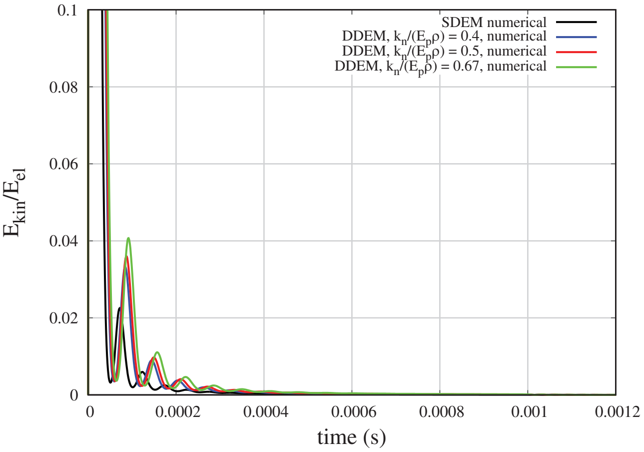

TABLE 1 Analytical deformable discrete element method solution for uniaxial compression of a cuboid specimen (the notation is explained in Appendix A)

E_p (N/m²)	$k_n/(E_p\rho)$ (–)	k' (N/m)	h' (N/m)	k'' (N/m)	h'' (m)	ΔH (m)	$u_x^{(i)}$ (m)
$1.5 \cdot 10^{11}$	0.667	$6.11 \cdot 10^{7}$	$1.64 \cdot 10^{-4}$	$6.77 \cdot 10^{7}$	$1.48 \cdot 10^{-4}$	$3.08 \cdot 10^{-3}$	$8.40 \cdot 10^{-5}$
$2.0 \cdot 10^{11}$	0.500	$6.77 \cdot 10^{7}$	$1.48 \cdot 10^{-4}$	$7.36 \cdot 10^{7}$	$1.36 \cdot 10^{-4}$	$2.78 \cdot 10^{-3}$	$6.30 \cdot 10^{-5}$
$2.5 \cdot 10^{11}$	0.400	$7.24 \cdot 10^{7}$	$1.38 \cdot 10^{-4}$	$7.77 \cdot 10^{7}$	$1.29 \cdot 10^{-4}$	$2.61 \cdot 10^{-3}$	$5.04 \cdot 10^{-5}$

FIGURE 10 Evolution of the displacement in the lateral direction—comparison of the standard and DDEM solutions, $k_n = 10^8$ N/m, $\nu_p = 0.33$. DDEM, deformable discrete element method

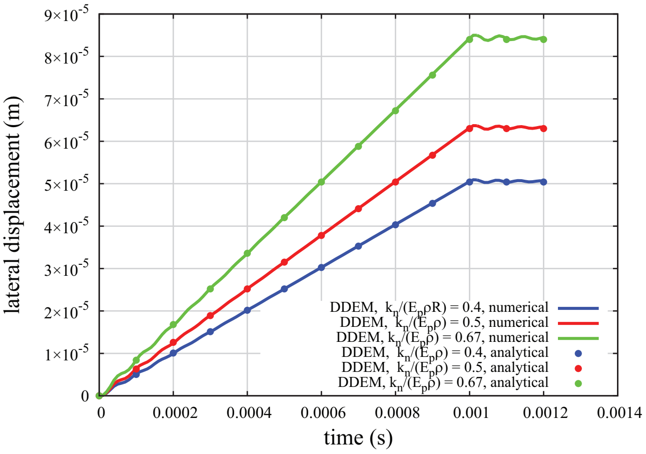

have been compared with the analytical solution according to Equation (A24). The lateral displacement $u_x^{(i)}$ for the final loading is given in Table 1. The analytical solution and the numerical predictions show a very good agreement.

The excellent agreement of the numerical predictions with the analytical solution for this simple benchmark confirms the correctness of the numerical implementation of the DDEM algorithm.

5.2 | Determination of micro–macro relationships for irregular configuration

In practical applications, discrete element models with irregular configurations of nonuniform sized particles are used. The performance of the DDEM for such models is studied next with the main objective to determine micro–macro relationships for the constitutive parameters in the elastic range.

An unconfined uniaxial compression of a cylindrical sample with diameter $D = 50$ mm and height $H = 50$ mm as shown in Figure 11 has been taken into account in the numerical studies. Two discrete element models (Figure 12) have been generated with the graphical preprocessor GiD[45] using the algorithm developed in Reference 46. This allowed to obtain densely packed particle assemblies with high coordination numbers.

Specimen 1 comprises 11,118 spherical particles of nonuniform size with an average (mean) radius of 1.116637 mm, a minimum radius of 0.39 mm and a maximum radius of 2.031 mm. Specimen 2 is formed by 28,811 spherical particles with radii being in the range of 0.363–1.41568 mm, and an average radius of 0.824765 mm. The parameters of the particle assemblies are summarized in Table 2. The particle size distributions of both specimens are represented graphically by the histograms in Figure 13.

It can be clearly seen in Figure 13 that the two specimens have different particle size dispersion. Specimen 2 has a significantly narrower particle size distribution than specimen 1. This is also confirmed quantitatively by the lower coefficient of variation of specimen 2 (COV = 0.174437) compared with that of specimen 1 (COV = 0.215397), cf. Table 2.

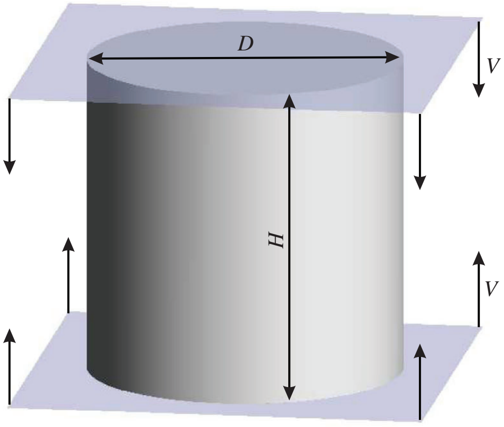

FIGURE 11 Uniaxial compression of a cylindrical specimen: Geometry and boundary conditions

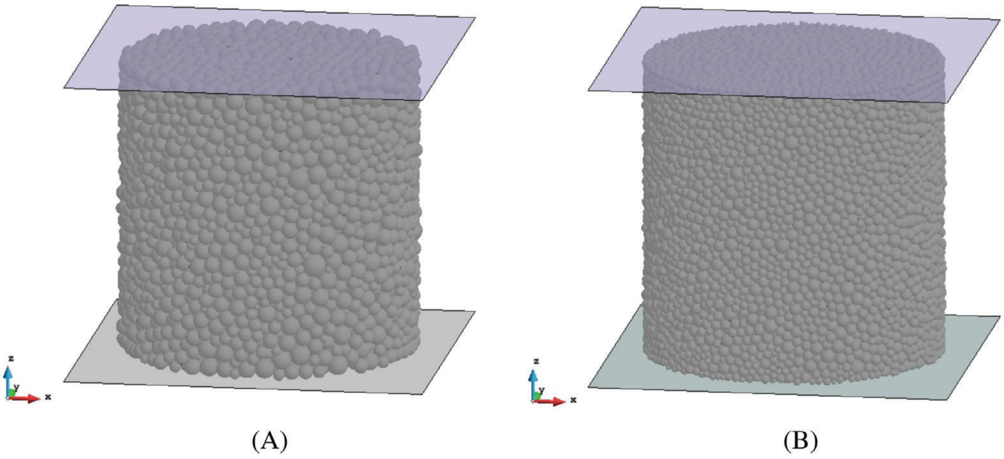

(A) (B)

FIGURE 12 Discrete element method models: (A) specimen 1 and (B) specimen 2

TABLE 2 Summary of discrete element method packing parameters for cylindrical specimens

Description	Specimen 1	Specimen 2
Number of particles, N_p	11,118	28,811
Mean radius, $\overline{\rho}$ (mm)	1.116637	0.824765
Minimum radius, $\rho_{\min}$ (mm)	0.390000	0.363000
Maximum radius, $\rho_{\max}$ (mm)	2.031000	1.415680
$\rho_{\max}/\rho_{\min}$	5.207692	3.899945
SD (mm)	0.240521	0.143870
Coefficient of variation, COV	0.215397	0.174437
Number of contacts, N_c	53,790	147,527
Coordination number, n_c	9.676201	10.241019
Porosity, e	0.246246	0.246694

FIGURE 13 Comparison of particle size distributions of the two specimens

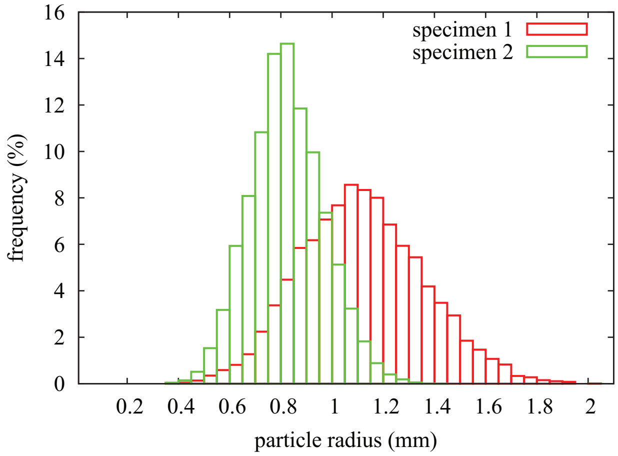

The dispersion can also be measured by the ratio $\rho_{\max}/\rho_{\min}$ and this ratio is also lower for specimen 2, cf. Table 2. The particle packing density is characterized by the average coordination number $n_c = 9.676201$ and 10.241019, for specimens 1 and 2, respectively. The porosity in the two DEM models is $e = 0.246246$ and 0.246694, for specimens 1 and 2, respectively.

The parameters of the DEM models for both specimens are given in Table 3. The problem has been analyzed using both the SDEM and DDEM. The loading has been introduced by the flat rigid plates moving with a constant velocity of 0.5 m/s and compressing the specimen through the contact. The plate–particle contact parameters are also given in Table 3. The response obtained with specimen 1 for both DEM models is represented by the compressive force plotted as a function of the total plate displacement in Figure 14. Both curves have been obtained for the stiffness ratio $k_t/k_n = 0.1$ and the deformable model specific parameters $E_p = 7 \cdot 10^{10}$ Pa and $\nu_p = 0.05$. The quasi-static regime of the process is confirmed by the plots of the ratio of kinetic energy to elastic strain energy in Figure 15. It can be observed that the ratio is far below 0.05 which was previously reported as the limit value for quasi-static conditions. The failure modes obtained under compressive loading using the SDEM and DDEM models are shown in Figure 16(A,B), respectively. Analogous results for specimen 2 are presented in Figures 17 and 18 for the ratio $k_t/k_n = 0.2$, and $E_p = 1.1 \cdot 10^{11}$ Pa and $\nu_p = 0.45$.

When comparing the force versus plate displacement curves for the SDEM and DDEM models in Figures 14 and 17, one can see a clear difference in their slope in the elastic range. This clearly shows how deformability of the particles can modify the elastic behavior of the material model. The curves obtained with both models in the failure and postfailure ranges have a similar character. Comparison of the failure modes in Figures 16 and 18 show similarities between the failure patterns for the standard and deformable models for both specimens. It is worth noting that the failure is more distributed in specimen 1. This is in agreement with the observations that more geometrically homogenous DEM models yield a more localized failure.[31]

TABLE 3 Parameters of the discrete element method model of uniaxial compression of the cylindrical sample

Parameter	Specimen 1	Specimen 2
Density, d (kg/m^3)	2780	2780
Contact bond normal stiffness, k_n (MN/m)	35	35
Contact stiffness ratio, k_t/k_n	$0 \div 1$	$0 \div 1$
Interparticle friction coefficient, μ	0.83	0.83
Contact bond normal strength, ϕ_n (N)	180	100
Contact bond shear strength, ϕ_t (N)	180	100
Particle-wall contact normal stiffness, $k_n^{(p-w)}$ (MN/m)	950	700
Particle-wall contact tangential stiffness, $k_n^{(p-w)}$ (MN/m)	950	700
Particle-wall friction coefficient, $\mu^{(p-w)}$	0.0	0.0
Translational damping factor, α_t	0.2	0.2
Rotational damping factor, α_r	0.2	0.2
Particle Young's modulus, E_p (Pa)	$7 \cdot 10^{10}$, $1 \cdot 10^{11}$	$9.47 \cdot 10^{10}$, $1.1 \cdot 10^{11}$
Particle Poisson's ratio, ν_p	0.05, 0.15, 0.25, 0.35, 0.45	0.05, 0.15, 0.25, 0.35, 0.45
Loading velocity, v (m/s)	0.5	0.5

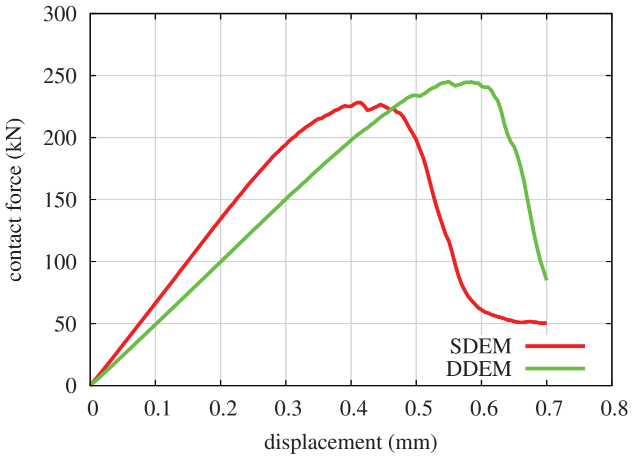

FIGURE 14 Comparison of the force versus plate displacement curves for specimen 1 for the SDEM and DDEM ($k_t/k_n = 0.1$, DDEM model: $E_p = 7 \cdot 10^{10}$ Pa, $\nu_p = 0.05$). DDEM, deformable discrete element method; SDEM, standard discrete element method

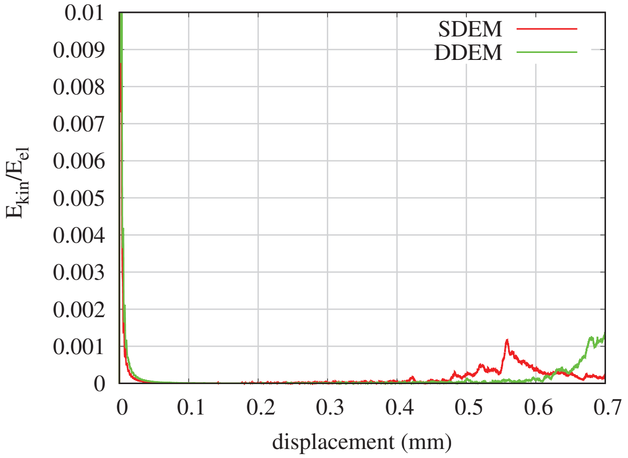

FIGURE 15 Ratio of kinetic energy to elastic strain energy in compression of specimen 1

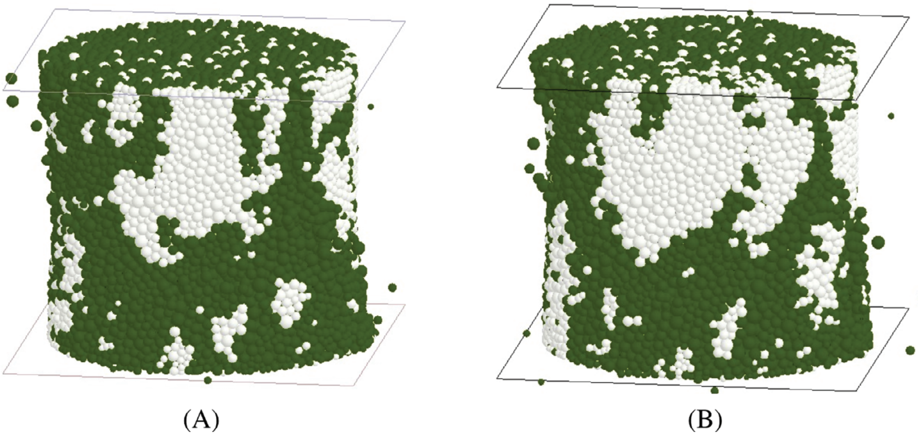

FIGURE 16 Predicted failure modes under unconfined uniaxial compression using specimen 1: (A) SDEM model, plate displacement 0.4 mm, and (B) DDEM model, plate displacement 0.55 mm. DDEM, deformable discrete element method; SDEM, standard discrete element method

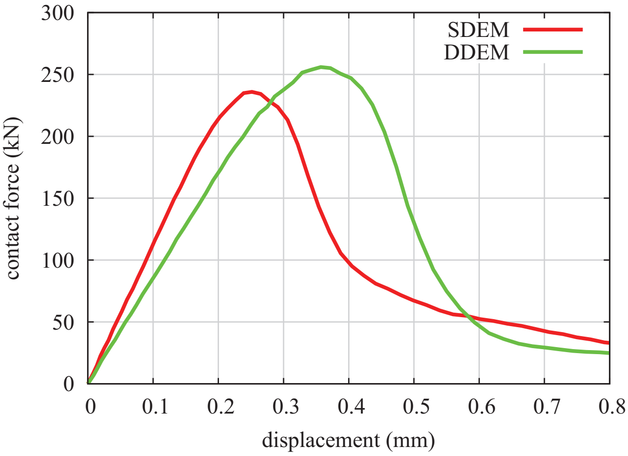

FIGURE 17 Comparison of the force versus plate displacement curves for specimen 2 for the SDEM and DDEM ($k_t/k_n = 0.2$, DDEM model: $E_p = 1.1 \cdot 10^{11}$ Pa, $\nu_p = 0.45$). DDEM, deformable discrete element method; SDEM, standard discrete element method

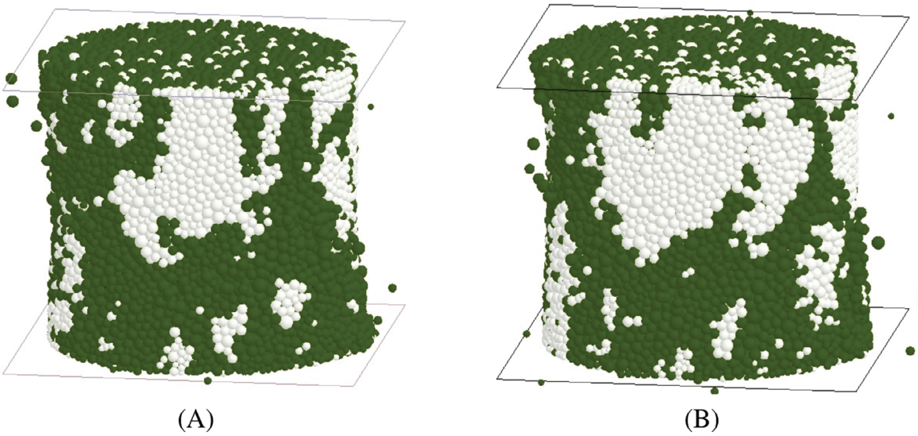

FIGURE 18 Predicted failure modes under unconfined uniaxial compression using specimen 2: (A) SDEM model and (B) DDEM model. DDEM, deformable discrete element method; SDEM, standard discrete element method

The simulations have been carried out on a personal computer with an Intel Xeon processor X5660 2.8 GHz. The CPU times of the SDEM simulations were 2 h 3 min and 7 h 31 min for specimens 1 and 2, respectively. The CPU times of the DDEM calculations were 3 h 22 min and 12 h 38 min for specimens 1 and 2. This corresponds to an increase of about 65%.

The effect of the microscopic model parameters on the macroscopic elastic properties have been investigated in detail. A series of numerical simulations using specimens 1 and 2 have been performed with different combinations of the dimensionless parameters k_t/k_n, $k_n/(E_p\bar{\rho})$, and ν_p to determine specific forms of the relationships (51) and (52) for the SDEM, and the relationships (53) and (54) for the DDEM. To ensure elastic behavior, possibility of bond breakage was blocked by setting very high values of bond strengths in the normal and tangential directions, ϕ_n and ϕ_t, respectively. The macroscopic Young's modulus E has been determined from the slope of the stress–strain curve (Figure 19) at a certain deformation range for which the response can be considered linear. The linearity can be checked using the linear correlation coefficient that measures the strength of the linear relationship between two variables.[47] The linear correlation coefficient for the data plotted in Figure 19 is 0.999677, which is very close to the ideal linear relationship with a correlation coefficient equal to 1. The same range of deformation has been used for evaluation of the Poisson's ratio ν. The evolution of the Poisson's ratio over time shown in Figure 20 has been carefully checked to reach a stable value. The stable value at the end of the analyzed interval has been taken as the corresponding macroscopic Poisson's ratio ν.

The axial stress plotted in Figure 19 has been evaluated using the contact force F as

$$\sigma_{zz} = \frac{F}{A}, \tag{55}$$

where A is the area of the base of the compressed cylindrical specimen, $A = \pi D^2/4 = 0.001963495\ \mathrm{m}^2$. The stress calculated in this way agrees very well with the one obtained from the averaging procedure according to Equation (42).

The macroscopic Poisson's ratio ν is given as the ratio of the strain components

$$\nu = -\frac{\varepsilon_r}{\varepsilon_a}. \tag{56}$$

The axial strain ε_a can be evaluated in terms of the plate displacement ΔH and the specimen height H:

$$\varepsilon_a = -\frac{\Delta H}{H}. \tag{57}$$

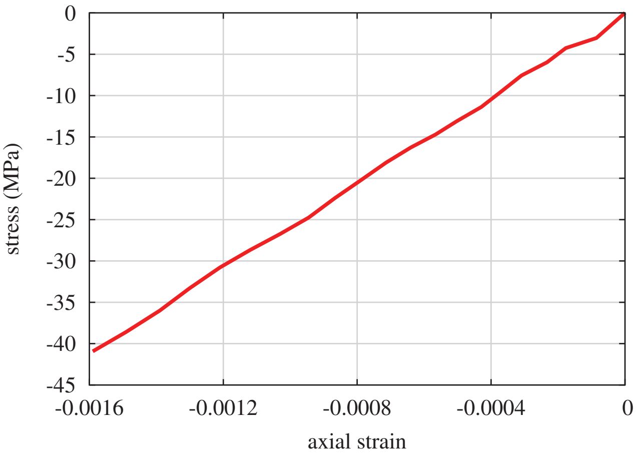

FIGURE 19 The stress–strain curve at the initial stage of loading for specimen 2, DDEM, $\nu_p = 0.45$, $k_t/k_n = 0.4$. DDEM, deformable discrete element method

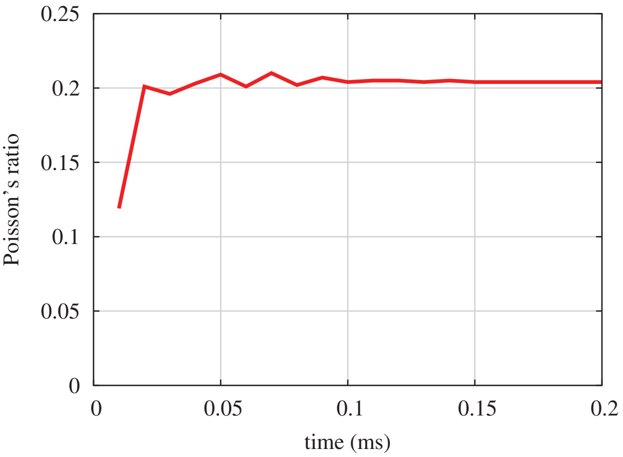

FIGURE 20 Evolution of the Poisson's ratio at the initial phase of loading for specimen 2, DDEM, $\nu_p = 0.45$, $k_t/k_n = 0.4$. DDEM, deformable discrete element method

However, accurate evaluation of the radial strain ε_r is not so easy. Therefore, both strain components have been evaluated employing the procedure proposed by Bagi[36] and outlined in Section 4.1, where the axial and radial strains have been taken from the components of the average strain tensor as follows:

$$\varepsilon_a = \varepsilon_{zz}, \quad \varepsilon_r = 0.5(\varepsilon_{xx} + \varepsilon_{yy}). \tag{58}$$

It was confirmed that the values of the components ε_{xx} and ε_{yy} were very close. Taking either of them as the radial strain instead of the average value did not considerably change the value of the Poisson's ratio.

The DEM and DDEM simulations have been performed using both specimens and taking the ratio k_t/k_n in the range from 0 to 1. The model parameters given in Table 3 have been used. The DDEM simulations have been run for different values of particle Poisson's ratio, namely, $\nu_p = 0.05$, 0.15, 0.25, 0.35 and 0.45, assuming a particle Young's modulus $E_p = 7 \cdot 10^{10}$ Pa for specimen 1 and $E_p = 9.47 \cdot 10^{10}$ Pa for specimen 2. This ensured the same value of the dimensionless parameter $k_n/(E_p\bar{\rho}) = 0.448$ for both specimens. For each case, the macroscopic Young's modulus E and Poisson's ratio ν have been evaluated.

The dimensionless scaling functions $\hat{\Phi}_E$ given by Equations (51) and (53) have been calculated using the coordination numbers n_c and porosities e from Table 2. The dimensionless scaling functions $\hat{\Phi}_\nu$ given by Equations (52) and (54) have also been determined. The dimensionless scaling functions $\hat{\Phi}_E$ and $\hat{\Phi}_\nu$ for both specimens for the DEM and DDEM models are shown in Figures 21 and 22.

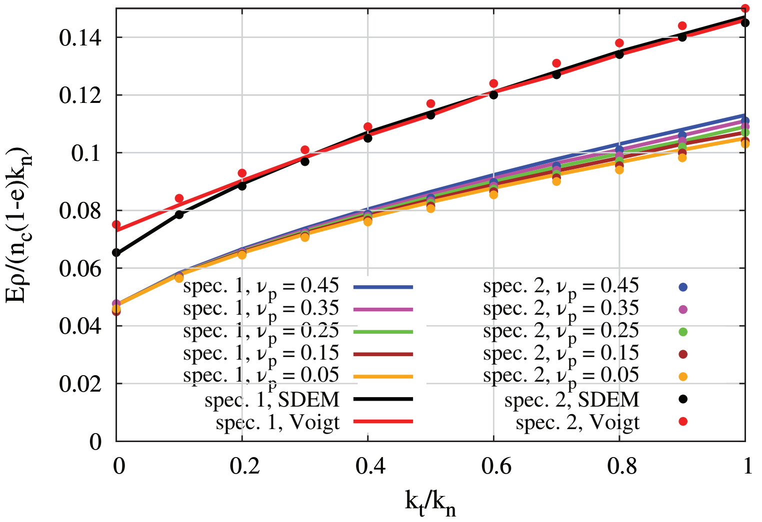

FIGURE 21 Micro–macro relationships between the dimensionless parameter $E\bar{\rho}/(k_n n_c(1-e))$ and the stiffness ratio k_t/k_n for different ν_p and for the fixed ratio $k_n/(E_p\bar{\rho}) = 0.448$

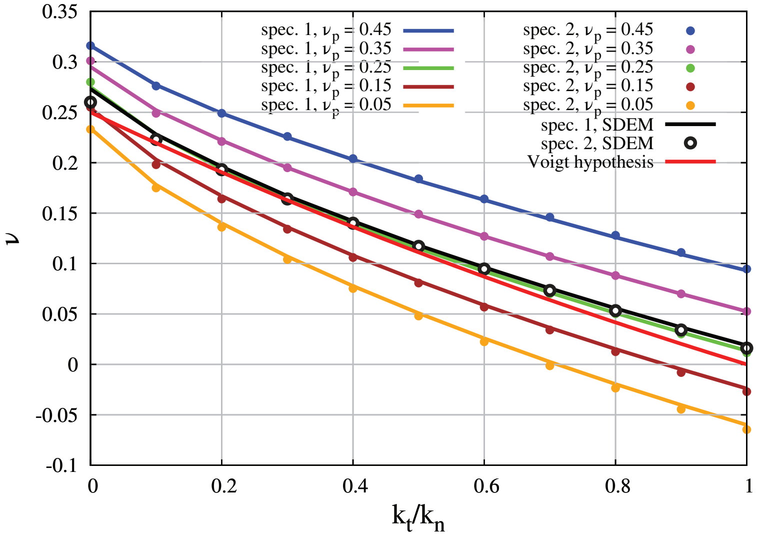

FIGURE 22 Micro–macro relationships between the macroscopic Poisson's ratio ν and the stiffness ratio k_t/k_n for different values of the particle Poisson's ratio ν_p for the fixed ratio $k_n/(E_p\bar{\rho}) = 0.448$

The numerical predictions in Figures 21 and 22 have been compared with analytical relationships making use of Equations (44) and (45) based on Voigt's hypothesis. The analytical values of Young's modulus E according to Equation (44) have been evaluated using the average square radius

$$\overline{\rho^2} = \frac{1}{N_p} \sum_{i=1}^{N_p} \rho_i^2, \tag{59}$$

which gives $\overline{\rho^2} = 1.30473 \cdot 10^{-6}\ \text{m}^2$ and $\overline{\rho^2} = 7.00936 \cdot 10^{-7}\ \text{m}^2$ for specimen 1 and 2, respectively. Other parameters necessary to obtain the analytical solutions are given in Tables 2 and 3. The numerical predictions obtained using the DEM models plotted in Figures 21 and 22 agree very well with the analytical solutions according to Voigt's hypothesis. This confirms an excellent performance of the models and DEM implementation. Furthermore, the respective relationships obtained with two different specimens are in good agreement, which shows that the dimensional analysis framework has been applied correctly.

Figure 21 allows us to see how the deformability of the particles affects the macroscopic stiffness. It can be seen that the DDEM gives a lower macroscopic stiffness than the SDEM, which was already noticed in the comparison of the force–displacement curves in Figures 14 and 17. Here, we can observe this effect over the full range of considered k_t/k_n ratios as well as for different particle Poisson's ratios ν_p. It can be seen that the influence of the particle Poisson's ratio ν_p on the macroscopic stiffness is quite small, especially for lower values of the ratio k_t/k_n. These observations are similar to those made for the 2D implementation of the DDEM.[22]

Figure 22 demonstrates that by using the DDEM a broader range of the values for the effective macroscopic Poisson's ratio can be obtained compared with the SDEM. Similarly as in the 2D DDEM formulation,[22] the curves representing the results from the DDEM simulations are offset with respect to the curve for the SDEM. The DDEM can give both higher and lower values of the Poisson's ratio compared with the SDEM. The curves corresponding to $\nu_p > 0.25$ are above the SDEM results, while those corresponding to $\nu_p < 0.25$ are below. Negative values of the macroscopic Poisson's ratio are obtained for larger values of the ratio, that is, $k_t/k_n > 1$, and lower values of the particle Poisson's ratio. Similarly, negative Poisson's ratios are predicted for the SDEM for $k_t/k_n > 1$, cf. Equation (45) and Reference 48. The DDEM model with $\nu_p = 0.25$ gives a Poisson's ratio which is practically the same as the SDEM. This was already observed and explained in the 2D DDEM formulation.[22]

The DDEM simulations for specimen 1 for values of particle Poisson's ratio $\nu_p = 0.05$, 0.25 and 0.45 have been rerun assuming a particle Young's modulus of $E_p = 1 \cdot 10^{11}$ Pa, which gives the dimensionless parameter $k_n/(E_p\overline{\rho}) = 0.313$.

The DDEM dimensionless relationships for different values of the particle Young's modulus E_p, and as a consequence different values of the dimensionless parameter $k_n/(E_p\overline{\rho})$, are shown in Figures 23 and 24. The results of the DDEM have been compared with the predictions of the SDEM, and these, in turn, with the theoretical estimations according to Voigt's hypothesis. Figure 23 demonstrates once more that the macroscopic stiffness in the DDEM is lower than in the SDEM. The lower the particle Young's modulus E_p (the higher the ratio $k_n/(E_p\overline{\rho})$), the lower the macroscopic stiffness represented by the dimensionless parameter $E\,\overline{\rho}/(k_n n_c(1-e))$.

Figure 24 allows us to analyse the effect of the particle Young's modulus E_p on the macroscopic Poisson's ratio ν. It can be seen that the lower the particle Young's modulus E_p (the higher the ratio $k_n/(E_p\overline{\rho})$), the bigger the change of the macroscopic Poisson's ratio ν with respect to the SDEM prediction. For a ratio $k_n/(E_p\overline{\rho})$ close to zero (for high values of the particle Young's modulus E_p) the DDEM solution converges to the SDEM solution.

The micro–macro relationships derived in terms of dimensionless parameters should be valid for the models with different values of dimensional parameters. For instance, the same value of the dimensionless parameter $E\,\overline{\rho}/(k_n n_c(1-e))$ should be obtained for different values of the particle Young's modulus E_p if the respective dimensionless parameters involving E_p are equal. In order to verify this, we perform simulations of the compression test using specimen 1 for three different values of particle Young's modulus E_p: 70, 7, and 0.7 GPa. To guarantee the similarity we use the contact stiffness values k_n of 35, 3.5, and 0.35 MN/m, and contact strength values ϕ_n of 180, 18, and 1.8 N. This ensures equality of the two dimensionless parameters: $k_n/(E_p\rho)$ and $k_n\rho/\phi_n$. The simulations have been performed for the contact stiffness ratio $k_t/k_n = 0.1$ and the particle Poisson's ratio $\nu_p = 0.05$. The axial stress versus axial strain curves for these three cases have are shown in Figure 25. It can be seen that the models with different micromechanical parameters give a different macroscopic stress. Figure 26 shows the same results but instead of the stress the dimensionless quantity $\sigma_{zz}\rho/k_n$ is used. It can be observed that the three plots coincide well with each other. This shows that a similar value of the dimensionless parameter involving the macroscopic Young's modulus $E\,\overline{\rho}/(k_n n_c(1-e))$ can be obtained from the three studied models.

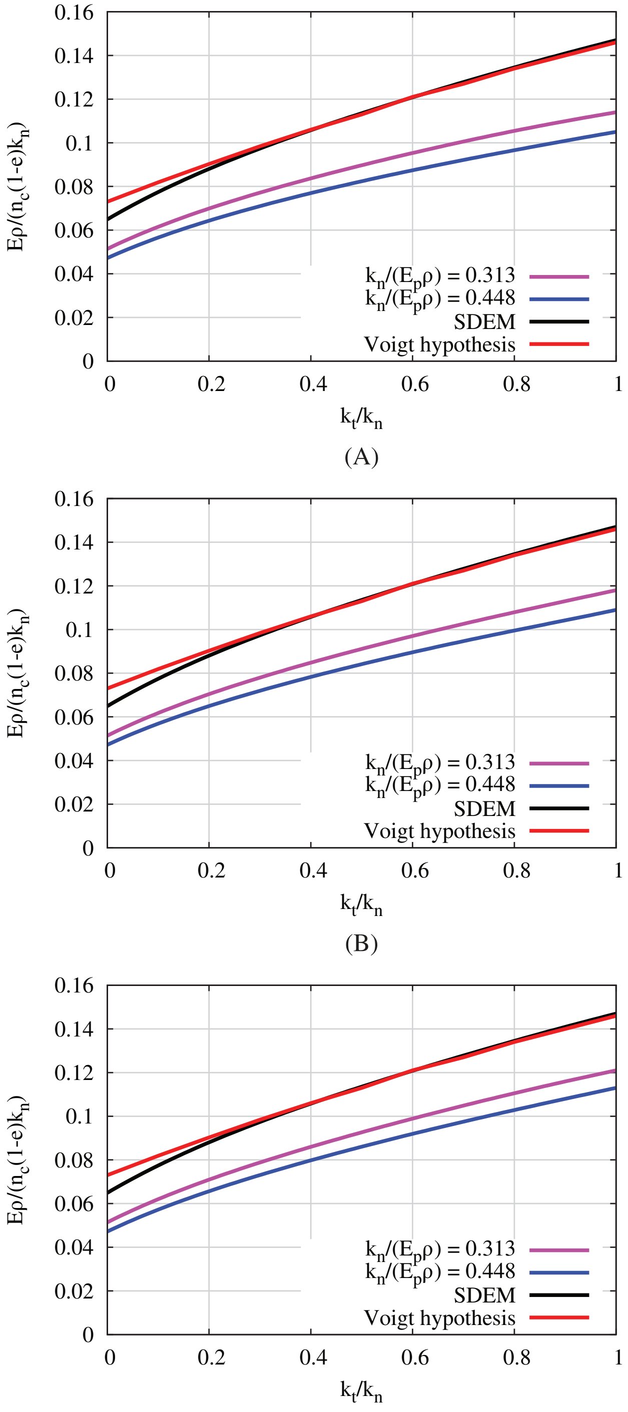

FIGURE 23 Micro–macro relationships between the dimensionless parameter $E\overline{\rho}/(k_n n_c(1-e))$ and the stiffness ratio k_t/k_n for different $k_n/(E_p\overline{\rho})$ and fixed ν_p: (A) $\nu_p = 0.05$, (B) $\nu_p = 0.25$, and (C) $\nu_p = 0.45$

6 | INVESTIGATION OF STABILITY OF THE DDEM SOLUTION

6.1 | Stability of solution for SC configuration

The stability of the DDEM applied to a regular SC particle configuration has been investigated numerically by simulations of the uniaxial compression tests of the cuboid specimen defined in Section 5.1. The results have been compared with the analytical convergence limits determined in Appendix B.

Similarly as in Section 5.1, normal contact stiffness and contact stiffness ratio have been set to $k_n = 1 \cdot 10^8$ N/m and $k_t/k_n = 0.0$, respectively. Numerical studies have been carried out assuming values of particle Poisson's ratio ν_p of 0.01,

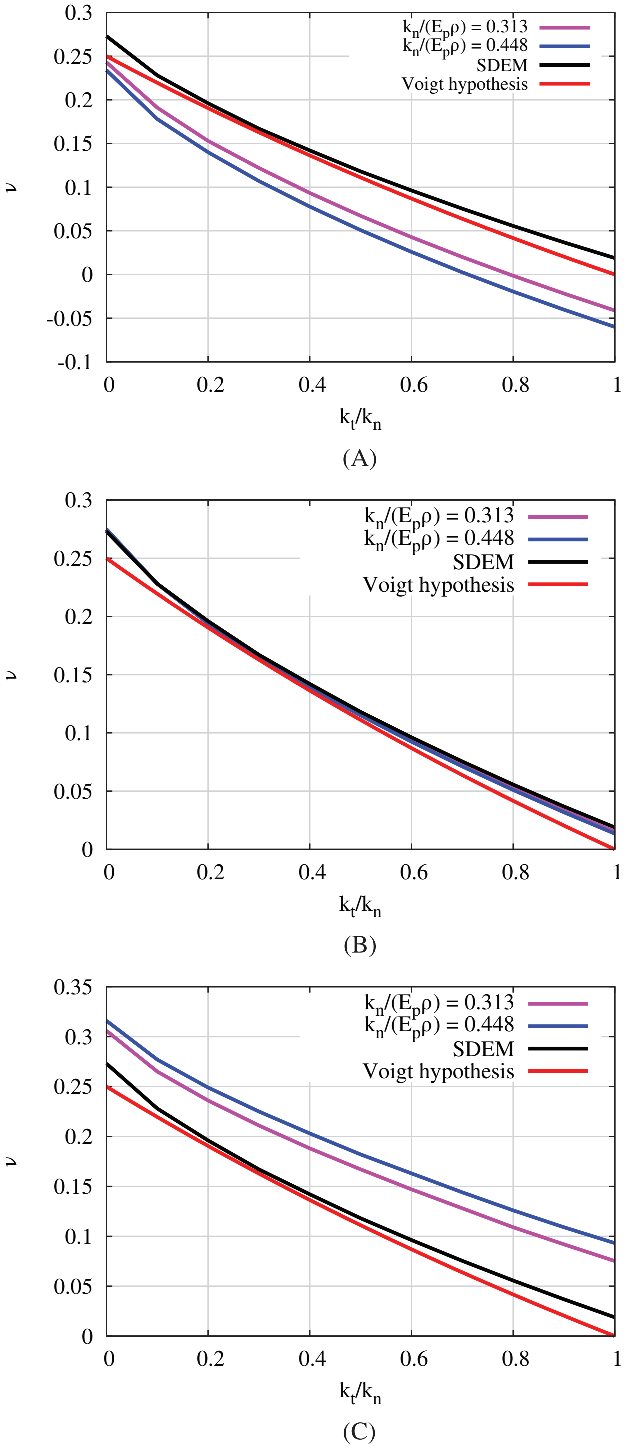

(A)

(B)

(C)

FIGURE 24 Micro–macro relationships between the macroscopic Poisson's ratio ν and the stiffness ratio k_t/k_n for different values of $k_n/(E_p\bar{\rho})$ and fixed ν_p: (A) $\nu_p = 0.05$, (B) $\nu_p = 0.25$, and (C) $\nu_p = 0.45$

0.1, 0.2, 0.3, 0.4, and 0.49 for checking the stability of solutions for different values of the particle Young's modulus E_p. The stability has been assessed by the appearance of the displacement field. Contours of displacements corresponding to stable solutions are presented in Figure 7, whereas the instability has been manifested by some anomalies such as those shown in Figure 27.

Figure 28 shows the stability limits in terms of Poisson's ratio ν_p and dimensionless parameter $k_n/(E_p\rho)$. The numerical predictions have been compared to the theoretical convergence limits for the iterative solution scheme determined according to Equation (B16). It can be seen that the numerical stability limits coincide to the theoretical predictions. This means that the stability of the explicit transient solution is also controlled by the convergence criterion of the iterative scheme.

FIGURE 25 Axial stress versus axial strain curves for specimen 1 and DDEM models with different stiffness and strength parameters ($k_t/k_n = 0.1$, $\nu_p = 0.05$). DDEM, deformable discrete element method

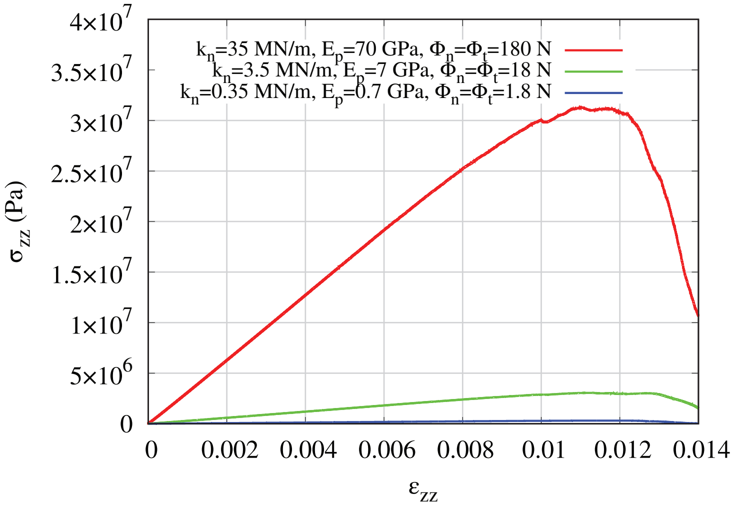

FIGURE 26 Dimensionless stress–strain relationships obtained with specimen 1 and DDEM models with different stiffness and strength parameters ($k_t/k_n = 0.1$, $\nu_p = 0.05$). DDEM, deformable discrete element method

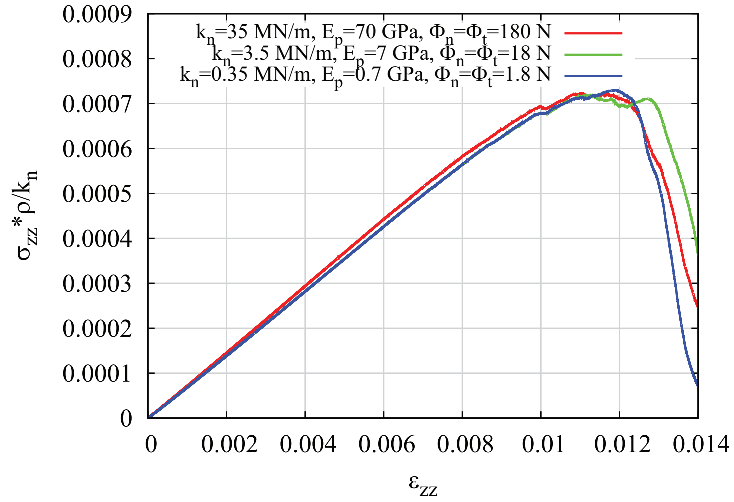

FIGURE 27 Unstable DDEM solution for SC configuration—contours of displacements (in meters) along the z-axis at $t = 1.1 \cdot 10^{-3}$ ms. DDEM, deformable discrete element method; SC, simple cubic

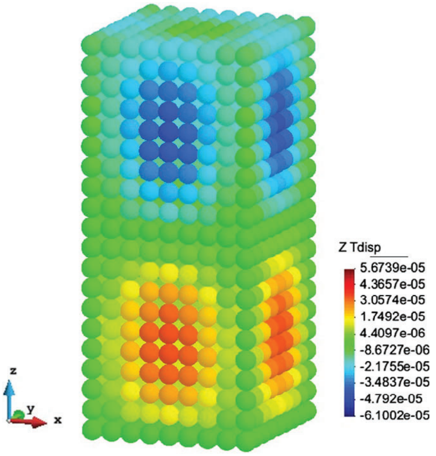

6.2 | Stability of the solution for the body centered cubic configuration

Numerical studies of the stability limit for the BCC (body centered cubic) configuration have been conducted using the specimen shown in Figure 29(A) composed of 19 layers of 1386 equal-sized bonded particles arranged in a BCC pattern. Similarly as in Section 6.1, we have particle radius $\rho = 1$ mm, normal contact stiffness $k_n = 1 \cdot 10^8$ N/m and the contact stiffness ratio $k_t/k_n = 0.0$. The specimen has been subjected to uniaxial compression induced by contact with two rigid plates. A contact stiffness $k_n = 1 \cdot 10^7$ N/m and zero friction between the particles and plates have been assumed. The loading has been introduced by the top plate moving downward with a constant velocity of 0.05 m/s while the bottom plate has been fixed. To ensure a quasi-static response, a damping coefficient of $\xi^n = 1.3$ at the contact has been used.

Numerical studies have been performed taking a certain value of particle Poisson's ratio ν_p in the range $0.01 \div 0.49$ and checking the stability of the solutions for different values of the particle Young's modulus E_p. The stability has been assessed by the appearance of the displacement field. Contours of displacements corresponding to a stable solution are presented in Figure 29(B), whereas the instability has been manifested by some anomalies such as those shown in Figure 29(C).

The results of the numerical stability analysis for the BCC configuration are given in Figure 30. The curve separating the stable and unstable zones is plotted together with similar curves obtained for irregular particle configuration obtained for specimens 1 and 2.

6.3 | Stability of the solution for an irregular particle configuration

Stability limits for irregular particle configurations under uniaxial compression have been investigated using specimens 1 and 2 introduced in Section 5.2. The simulations have been performed with $k_t/k_n = 0$.

Numerical studies have been carried out for particle Poisson's ratios ν_p in the range $0.01 \div 0.49$. For each value of the Poisson's ratio ν_p, the limit value of the particle Young's modulus E_p has been determined based on the displacement field. Contours of displacements in a stable and unstable solution are shown in Figure 31.

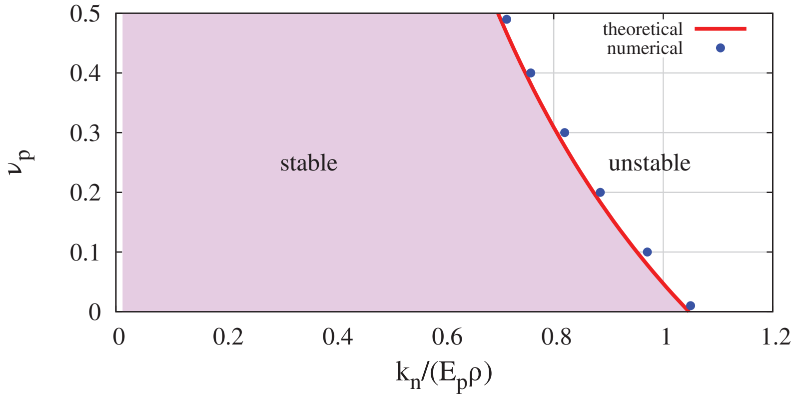

FIGURE 28 Stability limits for simple cubic configuration

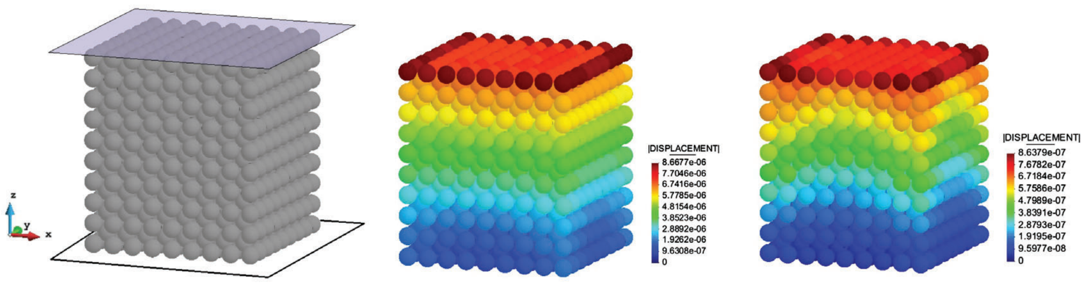

(A) (B) (C)

FIGURE 29 Analysis of body centered cubic configuration: (A) particle model, (B) contours of displacement magnitudes (in meters) in stable solution at $t = 1.2$ ms, and (C) contours of displacement magnitudes (in meters) in unstable solution at $t = 1.2$ ms

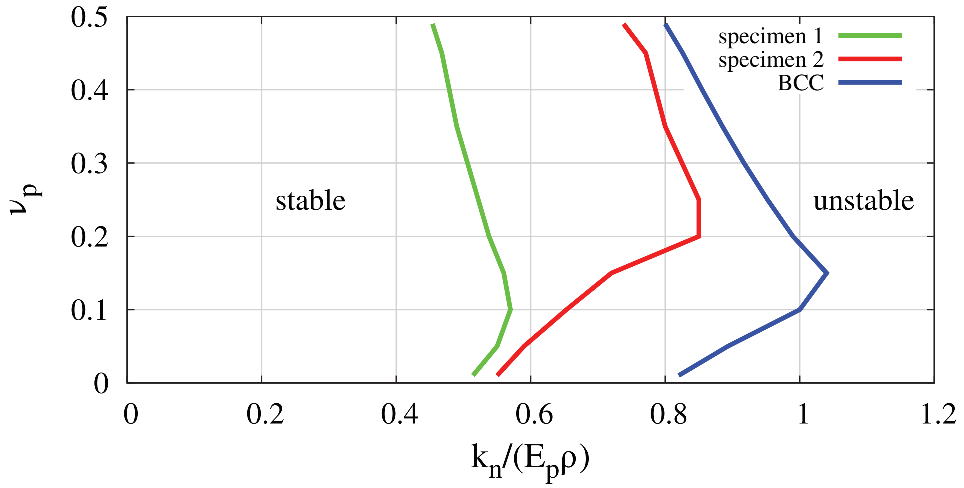

FIGURE 30 Stability limits for cylindrical specimen in comparison with body centered cubic limits

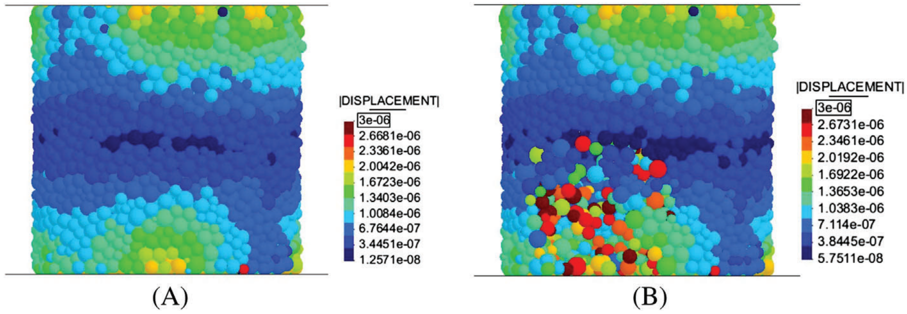

(A) (B)

FIGURE 31 Stability analysis of specimen 1: (A) Contours of displacement magnitudes (in meters) in stable solution at $t = 4.05 \cdot 10^{-2}$ ms, and (B) contours of displacement magnitudes (in meters) in unstable solution at $t = 4.05 \cdot 10^{-2}$ ms

The stability limits for both specimens are shown in Figure 30 in terms of particle Poisson's ratio ν_p and the dimensionless parameter $k_n/(E_p\overline{\rho})$. It can be seen that the stability limits of irregular configurations show a behavior similar to that of the BCC configuration, however, they are off-set by a certain value. This can be explained by the fact that the limits for specimens 1 and 2 are calculated using an average radius $\overline{\rho}$) in the ratio $k_n/(E_p\overline{\rho})$ while instability is induced locally and depends on a certain local value of $\rho < \overline{\rho}$. This also explains why the curve for the more homogeneous specimen 2 is closer to the curve corresponding to the BCC configuration. A local origin of the unstable behavior can be noticed in Figure 31(B).

7 | CONCLUDING REMARKS

The DDEM has been extended into 3D. The DDEM which was previously implemented and validated in 2D[22,23] has been adapted in a straightforward way to 3D problems taking spherical particles instead of cylindrical discs and full 3D representations of stress and strain tensors. The particles are treated as deformable. It is assumed that the particle deformation consists of both a global and a local deformation mode. The global deformation is due to the internal particle stress induced by the contact forces. The volume-averaged stress is evaluated for each particle, and the inverse constitutive relationship is used to calculate the particle strain defining the global deformation. The contact forces are evaluated as functions of the overlaps (and gaps if the particles are bonded) of globally deformed particles. These overlaps or gaps represent the local deformation of the particles at the contact area.

The contact forces at a given contact indirectly depend on the contact forces at other contacts which means that the contact model in the DDEM is nonlocal. This mitigates one of the weaknesses of the SDEM: the assumption of the locality of the contact between particles.

Numerical tests have confirmed a good performance of the developed algorithm. Simulation results for a cuboid specimen composed of particles aligned in the SC pattern have been compared with the analytical solution showing a very good agreement. Micro–macro relationships in the elastic range have been investigated. Numerical studies have proofed the enhancement of the modeling capabilities of the DDEM in comparison to the SDEM. It has been demonstrated that the DDEM broadens the range of the macroscopic Poisson's ratio, which can be achieved in a discrete model. The DDEM is able to capture the Poisson's effect even in simple regular configurations where the SDEM fails to reproduce this effect. The new formulation also affects Young's modulus. The equivalent Young's modulus decreases with respect to the SDEM. The SDEM model can be seen as a limit case of the DDEM model for very high particle stiffness.

The failure and postfailure behaviors have not been analyzed in detail, however, stress–strain curves and fractured specimens do show that the DDEM maintains the failure pattern, ductile or brittle, which is obtained in the SDEM. Although the present work has been focused on models with bonded particles the proposed formulation is also valid for unbonded particles.

The stability of the 3D DDEM algorithm has been studied. Similarly, as in Reference 23, it has been found that the convergence criterion of the accurate iterative scheme imposes an additional criterion for the stability of the explicit solution. The analytical convergence criterion has been found to perfectly agree with the stability limits obtained for the SC configuration. Stability limits have also been investigated numerically for the DDEM solution of the specimen with particles aligned according to the body centered cubic pattern and for specimens with irregular configurations. It has been found that the solution for the BCC configuration gives an assessment of the DDEM stability for irregular particle configurations. A better assessment is obtained for more geometrically homogeneous specimens.

The current formulation was developed for small strain elasticity. In principle, it can be extended to finite strain elasticity using appropriate stress and strain measures.[49] The stress tensor calculated according to Equation (22) can be considered the second Piola–Kirchhoff stress tensor. Then, using an inverse constitutive relationship for the second Piola–Kirchhoff stress tensor we can determine the Green-Lagrange strain tensor or the right Cauchy-Green deformation tensor and, subsequently, principal stretches which define the ellipsoid of the deformed configuration. This ellipsoid should be used in the evaluation of the new contact forces. It should be remarked that although the rotation is not considered in the elastic deformation of the particle, the rigid motion of the particle determined in the initial stage of the algorithm takes finite rotations into account. If deformations are large, the ellipsoidal shape should be considered in the evaluation of the inertia tensor and the general form of the equation of rotational motion should be used.

Finally, it should be noted that the presented approach is also valid for arbitrarily shaped particles since Equation (22) can still be used and the constitutive equation for the calculation of the strain, Equation (24), does not depend on the particle volume. Similarly, Equation (27) can be used to calculate the displacements of any point in an arbitrary domain with a uniform strain. Nevertheless, the adaptation of the algorithm to arbitrarily shaped discrete elements would require the use of a general form of the equation of rotational motion and an appropriate contact detection algorithm.

ACKNOWLEDGMENTS

The authors would like to acknowledge the financial support of the National Science Centre (DEC-2015/19/B/ST8/03983) and the Australian Research Council (DP190102407).

DATA AVAILABILITY STATEMENT

The data that support the findings of this study are available from the corresponding author upon reasonable request.

ORCID

Jerzy Rojek https://orcid.org/0000-0002-8709-4059
Klaus Thoeni https://orcid.org/0000-0001-7351-7447

REFERENCES

1. Plassiard JP, Belheine N, Donze FV. A spherical discrete element model: calibration procedure and incremental response. *Granul Matter*. 2009;11:293-306.
2. Martin CL, Bouvard D, Shima S. Study of particle rearrangement during powder compaction by the discrete element method. *J Mech Phys Solids*. 2003;51:667-693.
3. Wu T, Temizer I, Wriggers P. Computational thermal homogenization of concrete. *Cem Concr Compos*. 2013;35:59-70.
4. Potyondy DO, Cundall PA. A bonded-particle model for rock. *Int J Rock Mech Min Sci*. 2004;41:1329-1364.
5. Senapati R, Zhang J. Identifying fracture origin in ceramics by combination of nondestructive testing and discrete element analysis. *AIP Conf Proc*. 2010;1211(1):1445-1451.
6. Cundall PA, Strack ODL. A discrete numerical method for granular assemblies. *Geotechnique*. 1979;29:47-65.
7. Cundall PA. Distinct element models of rock and soil structure. *Analytical and Computational Models in Engineering and Rock Mechanics*. London, UK: Allen&Unwin; 1987.

8. Harthong B, Jérier J-F, Dorémus P, Imbault D, Donzé F-V. Modeling of high-density compaction of granular materials by the discrete element method. *Int J Solids Struct*. 2009;46:3357-3364.
9. Bathurst RJ, Rothenburg L. Micromechanical aspects of isotropic granular assemblies with linear contact interactions. *ASME J Appl Mech*. 1988;55:17-23.
10. Gethin DT, Lewis RW, Ransing RS. A discrete deformable element approach for the compaction of powder systems. *Model Simul Mater Sci Eng*. 2003;11:101-114.
11. Munjiza A. *The Combined Finite–Discrete Element Method*. Hoboken, NJ: Wiley; 2004.
12. Nezamabadi S, Nguyen TH, Delenne JY, Radjai F. Modeling soft granular materials. *Granul Matter*. 2017;19(8):1–12. https://doi.org/10.1007/s10035-016-0689-y.
13. Vu TL, Nezamabadi S, Barés J, Mora S. Analysis of dense packing of highly deformed grains. *EPJ Web Conf*. 2017;140:15031.
14. Dosta M, Costa C, Al-Qureshi H. Numerical investigation of compaction of deformable particles with bonded-particle model. *EPJ Web Conf*. 2017;140:15021.
15. Cundall PA, Maini T, Marti J, Beresford PJ, Last NC, Asgian MI. Computer modeling of jointed rock masses. U.S. Army Engineers Waterways Experiment Station, Technical Report N-78-4; 1978.
16. J.V. Lemos. Explicit codes in geomechanics – FLAC, UDEC and PFC. In L. Ribeiro e Sousa, E. Vargas Jr., M. Matos Fernandes, and Roberto Azevedo, editors, *Innovative Numerical Modelling in Geomechanics*, pages 299–315. CRC Press, Taylor & Francis, Boca Raton, FL: 2012.
17. Williams JR, Mustoe GW. Modal methods for the analysis of discrete systems. *Comput Geotech*. 1987;4:1-19.
18. Jin F, Zhang C, Hu W, Wang J. 3D mode discrete element method: elastic model. *Int J Rock Mech Min Sci*. 2011;48:59-66.
19. Shi GH. Discontinuous deformation analysis: a new numerical model for the statics and dynamics of deformable block structures. *Eng Comput*. 1992;9:157-168.
20. Brodu N, Dijksman JA, Behringer RP. Multiple-contact discrete-element model for simulating dense granular media. *Phys Rev E*. 2015;91:032201.
21. Karanjgaokar N. Evaluation of energy contributions using inter-particle forces in granular materials under impact loading. *Granul Matter*. 2017;19(36). https://doi.org/10.1007/s10035-017-0720-y.
22. Rojek J, Zubelewicz A, Madan N, Nosewicz S. The discrete element method with deformable particles. *Int J Numer Methods Eng*. 2018;114(8):828-860.
23. Madan N, Rojek J, Nosewicz S. Convergence and stability analysis of the deformable discrete element method. *Int J Numer Methods Eng*. 2019;118(8):320-344.
24. Munjiza A, Latham JP, John NWM. 3D dynamics of discrete element systems comprising irregular discrete elements – integration solution for finite rotations in 3D. *Int J Numer Methods Eng*. 2003;56:35-55.
25. O'Sullivan C, Bray JD. Modified shear spring formulation for discontinuous deformation analysis of particulate media. *J Eng Mech*. 2003;129:830-834.
26. Thornton C, Cummins SJ, Cleary PW. An investigation of the comparative behaviour of alternative contact force models during elastic collisions. *Powder Technol*. 2011;210:189-197.
27. Taylor LM, Preece DS. Simulation of blasting induced rock motion. *Eng Comput*. 1992;9(2):243-252.
28. Luding S. Micro-macro transition for anisotropic frictional granular packings. *Int J Solids Struct*. 2004;41(21):5821-5836.
29. Luding S. Macroscopic stress from dynamic rotating granular media. *AIP Conf Proc*. 2010;1227:208.
30. Rojek J, Karlis GF, Malinowski LJ, Beer G. Setting up virgin stress conditions in discrete element models. *Comput Geotech*. 2013;48:228-248.
31. Rojek J, Labra C, Su O, Onate E. Comparative study of different discrete element models and evaluation of equivalent micromechanical parameters. *Int J Solids Struct*. 2012;49:1497-1517.
32. Rojek J, Onate E, Labra C, Kargl H. Discrete element simulation of rock cutting. *Int J Rock Mech Mining Sci*. 2011;48:996-1010.
33. Rojek J, Zarate F, Agelet de Saracibar C, Gilbourne C, Verdot P. Discrete element modelling and simulation of sand mould manufacture for the lost foam process. *Int J Numer Meth Eng*. 2005;62(11):1421-1441.
34. Kelly CT. *Iterative Methods for Linear and Nonlinear Equations*. Philadelphia, PA: SIAM; 1995.
35. Kruyt NP, Rothenburg L. Micromechanical definition of strain tensor for granular materials. *ASME J Appl Mech*. 1996;118:706-711.
36. Bagi K. Analysis of microstructural strain tensors for granular assemblies. *Int J Solids Struct*. 2006;43:3166-3184.
37. Liao CL, Chang TP, Young DH. Stress-strain relationship for granular materials based on the hypothesis of best fit. *Int J Solids Struct*. 1997;34:4087-4100.
38. Fakhimi A, Villegas T. Application of dimensional analysis in calibration of a discrete element model for rock deformation and fracture. *Rock Mech Rock Eng*. 2007;40:193-211.
39. Huang H. *Discrete Element Modeling of Tool-Rock Interaction* [PhD thesis]. University of Minnesota; 1999.
40. Yang B, Jiao Y, Lei S. A study on the effects of microparameters on macroproperties for specimens created by bonded particles. *Eng Comput*. 2006;23(6):607-631.
41. Labra C. *Advances in the Development of the Discrete Element Method for Excavation Processes* [PhD thesis]. Polytechnic University of Catalonia; 2012.
42. da Cruz F, Emam S, Prochnow M, Roux J-N, Chevoir F. Rheophysics of dense granular materials: discrete simulation of plane shear flows. *Phys Rev E*. 2005;72:021309.
43. Rackauskaite E, Kotsovinos P, Rein G. Model parameter sensitivity and benchmarking of the explicit dynamic solver of LS-DYNA for structural analysis in case of fire. *Fire Saf J*. 2017;90:123-138.

44. Siswanto WA, Nagentrau M, Mohd Tobi AL, Tamin MN. Prediction of plastic deformation under contact condition by quasi-static and dynamic simulations using explicit finite element analysis. *J Mech Sci Technol*. 2016;30:5093-5101.
45. CIMNE. Gid: the personal pre and post processor; 2020. https://www.gidhome.com/.
46. Labra C, Onate E. High density sphere packing for discrete element method simulations. *Commun Numer Methods Eng*. 2009;25(7):837-849.
47. Z. Zhang and D. Shafer. *Introductory Statistics*. Boston, MA: Flatworld Knowledge; 2014.
48. Bathurst RJ, Rothenburg L. Note on a random isotropic granular material with negative Poisson's ratio. *Int J Eng Sci*. 1988;26:373-383.
49. Munjiza A, Rougier E, Knight EE. *Large Strain Finite Element Method. A Practical Course*. Hoboken, NJ: Wiley; 2015.
50. Bronshtein IN, Semendyayev KA. *Handbook of Mathematics*. Berlin, Heidelberg/Germany: Springer-Verlag; 1998.

How to cite this article: Rojek J, Nosewicz S, Thoeni K. 3D formulation of the deformable discrete element method. *Int J Numer Methods Eng*. 2021;122:3335–3367. https://doi.org/10.1002/nme.6666

APPENDIX A. ANALYTICAL SOLUTION OF A CUBOID SAMPLE WITH DEFORMABLE PARTICLES

The analytical solution of a cuboid sample with deformable particles arranged according to a SC pattern subjected to unconfined uniaxial compression investigated in Section 5.1 can be obtained analyzing a single column of the particle assembly as shown in Figure 5(A). The lateral interaction between the particles can be neglected since it is very small under unconfined boundary conditions. However, we do consider the deformability of the particles in the lateral direction and the resulting lateral deformation of the specimen.

Two different cases of contacting pairs will be distinguished in the solution. In the first one, shown in Figure A1(A), both contacting particles are internal ones, and in the other one, shown in Figure A1(B) one of the contacting particles occupies an extreme (either top or bottom) position in the column. The force interaction f between two contacting particles for both cases can be written as:

$$f = kh, \tag{A1}$$

where k is an equivalent normal contact stiffness between two deformable particles in contact and h is the overlap of the undeformed particles which according to Figure A1 can be expressed as

$$h = h_c + h_p^{(i)} + h_p^{(j)}, \tag{A2}$$

where $h_p^{(i)}$ and $h_p^{(j)}$ are the deflections of the ith and jth particles due to the deformability and h_c is the overlap between the two deformed particles.

The equivalent stiffness k can be determined considering the system of two deformable particles connected by three springs in series as shown in Figure A2.

The force transmitted through each spring is the same and can be evaluated as:

$$f = k_n h_c = k_p^{(i)} h_p^{(i)} = k_p^{(j)} h_p^{(j)}. \tag{A3}$$

Making use of the relationships of Equation (A3) in Equation (A2), the following relation can be obtained for the equivalent stiffness k

$$\frac{1}{k} = \frac{1}{k_n} + \frac{1}{k_p^{(i)}} + \frac{1}{k_p^{(j)}} \tag{A4}$$

which can be further written as

$$k = \frac{k_n k_p^{(i)} k_p^{(j)}}{k_n k_p^{(i)} + k_n k_p^{(j)} + k_p^{(i)} k_p^{(j)}}. \tag{A5}$$

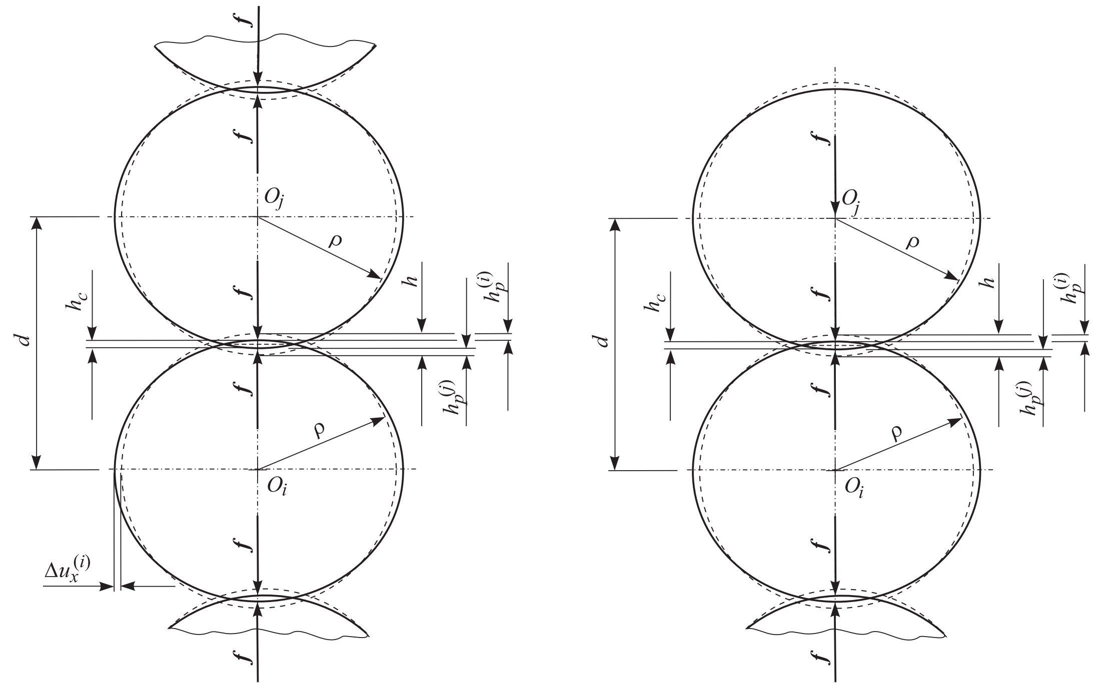

(A)

(B)

FIGURE A1 Column of spheres under compression: (A) Contact of internal particles and (B) contact with the particle at an extreme position in the column

FIGURE A2 Equivalent model for two deformable particles in contact

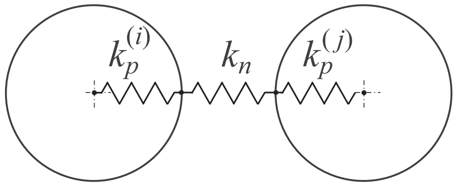

The stiffnesses $k_p^{(i)}$ and $k_p^{(j)}$ can be determined using the DDEM procedure. Using Equation (25) for the considered problem we have

$$(\varepsilon_p^{(i)})_{zz} = \frac{1}{E_p}(\sigma_p^{(i)})_{zz}. \tag{A6}$$

Calculating the average stress in the particle from Equation (22)

$$(\sigma_p^{(i)})_{zz} = \frac{2f\rho}{\frac{4}{3}\pi\rho^3} = \frac{3f}{2\pi\rho^2} \tag{A7}$$

and taking

$$(\varepsilon_p^{(i)})_{zz} = \frac{h_p^{(i)}}{\rho} \tag{A8}$$

we can rewrite Equation (A6) in the following form

$$f = \frac{2\pi E_p \rho}{3} h_p^{(i)} \tag{A9}$$

from which we can deduce

$$k_p^{(i)} = \frac{2\pi E_p \rho}{3}. \tag{A10}$$

The other particle stiffness $k_p^{(j)}$ will be determined separately for each distinguished case.

A.1 Internal pair of particles

When the jth particle is an internal one its stiffness is equal to the stiffness of the ith particle determined above, that is,

$$k_p^{(j)} = k_p^{(i)} \tag{A11}$$

and Equation (A5) can be simplified to

$$k = k' = \frac{k_n k_p^{(i)}}{2k_n + k_p^{(i)}}. \tag{A12}$$

Substituting Equation (A10) into Equation (A12) the equivalent stiffness k is given as follows:

$$k' = \frac{\pi E_p \rho k_n}{3k_n + \pi E_p \rho}. \tag{A13}$$

The overlap between the undeformed particles for the given force f can be evaluated as

$$h' = \frac{f}{k'}. \tag{A14}$$

A.2 Pair with one particle at an extreme position

When the jth particle is at the top of the column, the loading force does not contribute to the particle stress since it is applied to the particle center, and neither does the reaction force at the bottom of the column. The particle stress for the particle at the extreme position is evaluated as

$$(\sigma_p^{(j)})_{zz} = \frac{f\rho}{\frac{4}{3}\pi\rho^3} = \frac{3f}{4\pi\rho^2} \tag{A15}$$

which gives the relationship for the force

$$F = \frac{4\pi E_p \rho}{3} h_p^{(j)} \tag{A16}$$

and the particle stiffness

$$k_p^{(j)} = \frac{4\pi E_p \rho}{3} = 2k_p^{(i)}. \tag{A17}$$

With relationships (A17) and (A10), Equation (A5) takes the form

$$k = k'' = \frac{2k_n k_p^{(i)}}{3k_n + 2k_p^{(i)}} = \frac{4\pi E_p \rho k_n}{9k_n + 2\pi E_p \rho}. \tag{A18}$$

The corresponding overlap between the undeformed particles is given by

$$h'' = \frac{f}{k''}. \tag{A19}$$

The total change of height of the specimen of n_l layers can be evaluated as

$$\Delta H = (n_l - 3)h' + 2h''. \tag{A20}$$

The lateral deformation of the specimen is produced by the assumed deformation of the particles in the direction perpendicular to the loading direction. The particle lateral strain $(\varepsilon_p^{(i)})_{xx}$ for the internal particles is calculated as follows:

$$(\varepsilon_p^{(i)})_{xx} = -\nu_p(\varepsilon_p^{(i)})_{zz}. \tag{A21}$$

Inserting Equations (A6) and (A7) into Equation (A21) gives the following expression:

$$(\varepsilon_p^{(i)})_{xx} = -\nu_p \frac{3f}{2\pi E_p \rho^2}. \tag{A22}$$

The particle strain in the lateral direction can also be written as:

$$(\varepsilon_p^{(i)})_{xx} = \frac{\Delta u_x^{(i)}}{\rho}, \tag{A23}$$

where $\Delta u_x^{(i)}$ is the change of the particle radius in the lateral direction. Since no overlap between particles is assumed in the lateral direction and the lateral motion of the particles on the vertical plane of symmetry is restrained, the lateral displacement of the particles on the specimen sides is given as:

$$u_x^{(i)} = 8\Delta u_x^{(i)}. \tag{A24}$$

APPENDIX B. THEORETICAL CONVERGENCE ANALYSIS OF THE SC PARTICLE CONFIGURATION

We shall consider an infinite SC structure of equal spherical particles of radii ρ. We assume a prescribed uniform spacing d_x, d_y and d_z between the particles along the x, y, and z axes, respectively. The interparticle interaction is induced due to initial overlaps:

$$h_x = 2\rho - d_x \tag{B1}$$
$$h_y = 2\rho - d_y \tag{B2}$$
$$h_z = 2\rho - d_z \tag{B3}$$

where $h_x, h_y, h_z > 0$. Each particle in the SC structure contacts six other particles (Figure B1) Let the contact forces acting on the central particle be represented as $\mathbf{f}_c^i$, $i = 1, \ldots, 6$. In terms of their magnitudes f_i, $i = 1, \ldots, 6$, the contact force vectors are given as, $\mathbf{f}_c^1 = \begin{bmatrix} -\mathrm{f}_1 & 0 & 0 \end{bmatrix}^T$, $\mathbf{f}_c^2 = \begin{bmatrix} 0 & -\mathrm{f}_2 & 0 \end{bmatrix}^T$, $\mathbf{f}_c^3 = \begin{bmatrix} \mathrm{f}_3 & 0 & 0 \end{bmatrix}^T$, $\mathbf{f}_c^4 = \begin{bmatrix} 0 & \mathrm{f}_4 & 0 \end{bmatrix}^T$, $\mathbf{f}_c^5 = \begin{bmatrix} 0 & 0 & -\mathrm{f}_5 \end{bmatrix}^T$, $\mathbf{f}_c^6 = \begin{bmatrix} 0 & 0 & \mathrm{f}_6 \end{bmatrix}^T$. Making use of the symmetry of the pattern and loading we have $f_1 = f_3 = f_x$, $f_2 = f_4 = f_y$, and $f_5 = f_6 = f_z$.

The iterative procedure to find a converged solution at time step n can be presented as follows:

1. Calculate the stresses using the forces of the previous iteration

$$\begin{bmatrix} \sigma_{xx}^{(n,k)} \\ \sigma_{yy}^{(n,k)} \\ \sigma_{zz}^{(n,k)} \end{bmatrix} = -\frac{3}{2\pi\rho^2} \begin{bmatrix} f_x^{(n,k-1)} \\ f_y^{(n,k-1)} \\ f_z^{(n,k-1)} \end{bmatrix}. \tag{B4}$$

The superscript n denotes the time step and $k-1$, k, $k+1$ represent the successive iterations. It should be remarked that in this case $\sigma_{xy} = \sigma_{xz} = \sigma_{yz} = 0$.

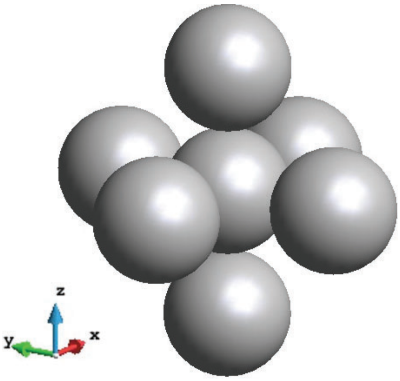

FIGURE B1 Simple cubic unit cell

2. Calculate the particle strains

$$\begin{bmatrix} \varepsilon_{xx}^{(n,k)} \\ \varepsilon_{yy}^{(n,k)} \\ \varepsilon_{zz}^{(n,k)} \end{bmatrix} = \frac{1}{E_p} \begin{bmatrix} 1 & -\nu_p & -\nu_p \\ -\nu_p & 1 & -\nu_p \\ -\nu_p & -\nu_p & 1 \end{bmatrix} \begin{bmatrix} \sigma_{xx}^{(n,k)} \\ \sigma_{yy}^{(n,k)} \\ \sigma_{zz}^{(n,k)} \end{bmatrix}. \tag{B5}$$

3. Calculate the global particle deformation defined by the semiaxes of the ellipsoid

$$\begin{bmatrix} a_{xx}^{(n,k)} \\ a_{yy}^{(n,k)} \\ a_{zz}^{(n,k)} \end{bmatrix} = \rho \begin{bmatrix} 1+\varepsilon_{xx}^{(n,k)} \\ 1+\varepsilon_{yy}^{(n,k)} \\ 1+\varepsilon_{zz}^{(n,k)} \end{bmatrix}. \tag{B6}$$

4. Calculate the particle overlaps in x, y, and z directions (local deformation)

$$\begin{bmatrix} h_{cx}^{(n,k)} \\ h_{cy}^{(n,k)} \\ h_{cz}^{(n,k)} \end{bmatrix} = 2\rho \begin{bmatrix} 1+\varepsilon_{xx}^{(n,k)} \\ 1+\varepsilon_{yy}^{(n,k)} \\ 1+\varepsilon_{zz}^{(n,k)} \end{bmatrix} - \begin{bmatrix} d_x \\ d_y \\ d_z \end{bmatrix} = \begin{bmatrix} h_x \\ h_y \\ h_z \end{bmatrix} + 2\rho \begin{bmatrix} \varepsilon_{xx}^{(n,k)} \\ \varepsilon_{yy}^{(n,k)} \\ \varepsilon_{zz}^{(n,k)} \end{bmatrix}. \tag{B7}$$

5. Calculate the new values of the contact force components

$$\begin{bmatrix} f_x^{(n,k)} \\ f_y^{(n,k)} \\ f_z^{(n,k)} \end{bmatrix} = k_n \begin{bmatrix} h_{cx}^{(n,k)} \\ h_{cy}^{(n,k)} \\ h_{cz}^{(n,k)} \end{bmatrix}. \tag{B8}$$

Substituting Equations (B7) and (B5) into Equation (B8) gives

$$\begin{bmatrix} f_x^{(n,k)} \\ f_y^{(n,k)} \\ f_z^{(n,k)} \end{bmatrix} = k_n \begin{bmatrix} h_x \\ h_y \\ h_z \end{bmatrix} + \frac{2\rho k_n}{E_p} \begin{bmatrix} 1 & -\nu_p & -\nu_p \\ -\nu_p & 1 & -\nu_p \\ -\nu_p & -\nu_p & 1 \end{bmatrix} \begin{bmatrix} \sigma_{xx}^{(n,k)} \\ \sigma_{yy}^{(n,k)} \\ \sigma_{zz}^{(n,k)} \end{bmatrix} \tag{B9}$$

and taking into account Equation (B4)

$$\begin{bmatrix} f_x^{(n,k)} \\ f_y^{(n,k)} \\ f_z^{(n,k)} \end{bmatrix} = k_n \begin{bmatrix} h_x \\ h_y \\ h_z \end{bmatrix} + \frac{3k_n}{\pi E_p \rho} \begin{bmatrix} 1 & -\nu_p & -\nu_p \\ -\nu_p & 1 & -\nu_p \\ -\nu_p & -\nu_p & 1 \end{bmatrix} \begin{bmatrix} f_x^{(k-1)} \\ f_y^{(k-1)} \\ f_z^{(k-1)} \end{bmatrix}. \tag{B10}$$

The relationship between successive differences can be obtained, as a specific form of Equation (38):

$$\begin{bmatrix} f_x^{(n,k+1)} - f_x^{(n,k)} \\ f_y^{(n,k+1)} - f_y^{(n,k)} \\ f_z^{(n,k+1)} - f_z^{(n,k)} \end{bmatrix} = \frac{3k_n}{\pi E_p \rho} \begin{bmatrix} 1 & -\nu_p & -\nu_p \\ -\nu_p & 1 & -\nu_p \\ -\nu_p & -\nu_p & 1 \end{bmatrix} \begin{bmatrix} f_x^{(n,k)} - f_x^{(n,k-1)} \\ f_y^{(n,k)} - f_y^{(n,k-1)} \\ f_z^{(n,k)} - f_z^{(n,k-1)} \end{bmatrix}. \tag{B11}$$

The iteration matrix **B** now takes the form:

$$\mathbf{B} = \frac{3k_n}{\pi E_p \rho} \begin{bmatrix} 1 & -\nu_p & -\nu_p \\ -\nu_p & 1 & -\nu_p \\ -\nu_p & -\nu_p & 1 \end{bmatrix}. \tag{B12}$$

In order to evaluate the convergence criterion in Equation (39) we calculate the spectral radius of the matrix **B** using Equation (40):

$$\rho(\mathbf{B}) = \max_{\lambda \in \Phi(\mathbf{B})} |\lambda|, \tag{B13}$$

where $\Phi(\mathbf{B})$ is the set of eigenvalues of the iteration matrix **B**

$$\Phi(\mathbf{B}) = \left\{ \frac{3k_n(1+\nu_p)}{\pi E_p \rho}, \frac{3k_n(1+\nu_p)}{\pi E_p \rho}, \frac{3k_n(1-2\nu_p)}{\pi E_p \rho} \right\} \tag{B14}$$

which have been determined analytically solving the cubic characteristic equation according to Reference 50. Since $\nu_p > 0$, the maximum eigenvalue and the spectral radius of the matrix **B** is given by

$$\rho(\mathbf{B}) = \max_{\lambda \in \Phi(\mathbf{B})} |\lambda| = \frac{3k_n(1+\nu_p)}{\pi E_p \rho}. \tag{B15}$$

Hence, it can be concluded that the convergence criterion for the iterative scheme is:

$$\frac{3k_n(1+\nu_p)}{\pi E_p \rho} < 1. \tag{B16}$$

Rewriting Equation (B16) we obtain a relationship for the particle Poisson's ratio ν_p in terms of the ratio $k_n/(E_p\rho)$ in the following form:

$$\nu_p < \frac{\pi/3}{k_n/(E_p\rho)} - 1. \tag{B17}$$